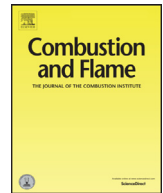




ELSEVIER

Contents lists available at ScienceDirect

Combustion and Flame

journal homepage: www.elsevier.com/locate/combustflame

A flamelet LES of turbulent dense spray flame using a detailed high-resolution VOF simulation of liquid fuel atomization

Jian Wen^{a,*}, Yong Hu^b, Takayuki Nishiie^c, Jun Iino^c, Assaad Masri^d, Ryoichi Kurose^a

^a Department of Mechanical Engineering and Science, Kyoto University, Kyoto daigaku-Katsura, Nishikyo-ku, Kyoto 615-8540, Japan

^b State Key Laboratory of Fire Science, University of Science and Technology of China, Hefei, Anhui 230026, China

^c Numerical Flow Designing Ltd., Higashigotanda, 1-10-10, Shinagawa City, Tokyo 141-0022, Japan

^d School of Aerospace Mechanical and Mechatronic Engineering, The University of Sydney, NSW 2006, Australia

ARTICLE INFO

Article history:

Received 8 May 2021

Revised 6 September 2021

Accepted 6 September 2021

Available online 28 September 2021

Keywords:

Atomization

Dense spray combustion

LES

Flamelet

E-L transformation

Needle spray burner

ABSTRACT

A numerical framework used to model dense spray flames is proposed. In this framework, the liquid fuel (acetone) atomization is solved by a detailed high-resolution VOF simulation, and the Eulerian components of liquid droplets are transformed into Lagrangian droplets, which are stored in a database at a certain downstream cross-section. Then, the combustion process is solved by a LES/FPV (flamelet progress variable) adopting the pre-stored database of Lagrangian droplets (i.e., the position, size, and velocity of each droplet) as the inlet boundary conditions. This framework is a one-way coupling between a VOF simulation and a combustion simulation. The validity of this approach is investigated by comparing the computations with the experiments of the Sydney Piloted Needle Spray Burner. The VOF simulation shows that the volume flux of the droplets at the nozzle exit fluctuates both temporally and spatially and the larger droplets tend to be located away from the center axis compared to the small droplets. The computed breakup length is in good agreement with the empirical correlation. In the database of the Lagrangian droplets for the LES/FPV of spray flames, the location of the sampling cross-section, the sampling time, and the threshold value for Eulerian–Lagrangian (E-L) transformation strongly affect the properties of the Lagrangian droplets, and are critical for the successful use of the LES/FPV. Two spray flames with different recess distances are computed using their optimal pre-stored droplets databases and both show generally good agreement with the experiments in terms of the gas temperature and droplet size distributions. The spray flame with a longer recess distance, which is more representative of a dilute spray, is considered to have a longer and wider premixed core than that with a shorter recess distance representing a dense spray. The discrepancy in the prediction of denser spray flames becomes more evident leading to over-predictions of gas temperature further downstream. Reasons for this behavior are discussed in the text.

© 2021 The Authors. Published by Elsevier Inc. on behalf of The Combustion Institute.

This is an open access article under the CC BY-NC-ND license

(<http://creativecommons.org/licenses/by-nc-nd/4.0/>)

1. Introduction

Owing to the increasing concerns regarding global warming and a shortage of energy, it is important for energy generators to achieve a high combustion efficiency and extremely low emissions. Therefore, liquid fuel spray combustion, which is widely used in gas turbine, gasoline, diesel, and rocket engines, merits detailed investigations. Spray combustion includes extremely complex physical phenomena, starting from the liquid fuel atomization along with the droplet evaporation and evaporated fuel-air mixing, end-

ing up with combustion. Therefore, the complexity involved makes it difficult to clarify the detailed mechanism and relevant models underlying spray atomization and combustion.

As mentioned by Masri [1], studies on spray combustion are generally classified into dense and dilute sprays. In the latter case, the spray dynamics associated with atomization is neglected. In a dense spray region where atomization occurs, many generated droplets make it difficult for experimental diagnostics to acquire sufficient information [2], thereby leaving the atomization process unclarified, and hence the dense spray region remains vague numerically [e.g., 3–30] and experimentally [e.g., 31,32–37,38]. For dilute spray flames, fuel sprays are regarded as a cluster of individual droplets and are then solved by the Lagrangian approach to

* Corresponding author.

E-mail address: wen.jen.66m@st.kyoto-u.ac.jp (J. Wen).

consider an interaction with the surrounding gas phase. However, the Lagrangian approach still has difficulty in providing the initial droplet size distribution near the nozzle exit owing to the abundance of interplayed phenomena, namely, the processes of primary breakup, secondary breakup, and droplet coalescence/collision [e.g., 39,40–46,47].

To investigate such spray combustion located in the dense regime, Masri et al. [e.g., 48,49,50] at the University of Sydney designed a canonical platform that can supply various spray inlet conditions, which is called the Sydney Piloted Needle Spray Burner (referred to as the Sydney Burner, hereafter) to stabilize repeatable turbulent spray flames by placing two concentric tubes within the pilot annulus. By varying the recess distance, which refers to the distance between the liquid fuel jet nozzle to the pilot outlet, different types of sprays can be reproduced. However, there haven't been any attempts to use a numerical simulation to couple the combustion process with the beginning atomization process together.

The purpose of this study is, therefore, to propose a numerical framework to model the coupling of atomization and combustion of dense spray flames while maintaining reasonable computational cost. Results are compared with experimental data obtained from the Sydney needle burner [49,50]. The concept is as follows. The liquid fuel atomization is solved by a detailed numerical simulation, in which both continuum gas and liquid phases are strictly solved in a Eulerian framework, and the Eulerian components of the liquid droplets are transformed into the Lagrangian droplets at a certain downstream cross-section, i.e., sampling cross-section, whose information is stored in database. Then, the combustion process is solved by a large eddy simulation (LES) with a flamelet model adopting the pre-stored database of Lagrangian droplets, namely, by a one-way coupling between a VOF simulation and a combustion simulation.

2. Mathematical models

In this work, all computations are performed using an unstructured LES solver, i.e., the FrontFlow/Red extended by Kyoto University [23,51,52].

2.1. Governing equations for dense spray region

In the dense spray region where the atomization process occurs, liquid and gas continuum phases are treated as incompressible fluids and are both solved in a Eulerian framework. Their governing equations solved in this region include the conservation equations of mass and momentum as follows,

$$\rho \nabla \cdot \mathbf{u} = 0, \quad (1)$$

$$\rho \left(\frac{\partial \mathbf{u}}{\partial t} + \mathbf{u} \cdot \nabla \mathbf{u} \right) = -\nabla P + \nabla \cdot (2\mu \mathbf{S}) + \mathbf{F}_\sigma + \mathbf{g}. \quad (2)$$

Here, ρ is the local density, \mathbf{u} the velocity vector, P the pressure, μ the viscosity, \mathbf{S} the rate-of-strain tensor $S_{ij} \equiv (\partial_i u_j + \partial_j u_i)/2$, and \mathbf{F}_σ is the source term of surface tension calculated by the continuum surface force (CSF) model [53].

The high-resolution interface capturing (HRIC) scheme [54] is implemented into the volume of fluid (VOF) method in order to capture the gas-liquid interface and the atomization process, where the VOF advection function takes the following form Albadawi et al. [55],

$$\frac{\partial \psi}{\partial t} + \mathbf{u} \cdot \nabla \psi + u_m \cdot \nabla [(1 - \psi)(\psi)] = 0, \quad (3)$$

where, ψ is the VOF value within each grid, and $\mathbf{u}_m = \mathbf{u}_l - \mathbf{u}_g$ is the compressive velocity. The subscripts l and g refer to liquid and

gas phases, respectively. The compressive velocity is considered only for the gas-liquid interface in the normal direction to avoid a dispersion of the VOF value. This additional compressive term helps retain the mass conservation and convergence for the VOF advection. It also facilitates the simulation of a multiphase flow with a large liquid/gas density ratio. Because the present study is performed in cylindrical coordinates with unstructured grids, the HRIC scheme is implemented instead of the coupled level-set and VOF method, which avoids the unnecessary complexity induced by the use of the level-set method.

A tagging method [56] is then utilized to transform the Eulerian liquid parts at a specific downstream cross-section into the Lagrangian spherical droplets with the droplet properties such as the position, size, and velocity, which are saved in a database (referred to as E-L tagging and E-L transformation, respectively, hereafter). Then, the stored Lagrangian droplets are utilized as the inlet boundary conditions for the combustion process.

2.2. Governing equations for dilute spray region

The combustion process occurring in the dilute spray region is modeled by a LES, utilizing the governing equations for the mass, momentum, and energy, and the detailed information can be found in studies [24,28,30]. To include the detailed chemical kinetics, a non-adiabatic version of flamelet/progress variable approach (FPV) [52,57] is used for the modeling of the turbulence-chemistry interaction, which results in the solution of the following equations,

$$\frac{\partial \bar{\rho}}{\partial t} + \nabla \cdot (\bar{\rho} \tilde{\mathbf{u}}) = S_\rho, \quad (4)$$

$$\frac{\partial \bar{\rho} \tilde{\mathbf{u}}}{\partial t} + \nabla \cdot (\bar{\rho} \tilde{\mathbf{u}} \tilde{\mathbf{u}}) = -\nabla \bar{P} + \nabla \cdot (\tilde{\boldsymbol{\tau}} + \tilde{\boldsymbol{\tau}}_{sgs}) + S_{\rho u}, \quad (5)$$

$$\frac{\partial \bar{\rho} \tilde{h}}{\partial t} + \nabla \cdot (\bar{\rho} \tilde{\mathbf{u}} \tilde{h}) = \nabla \cdot [\bar{\rho} (\tilde{D}_h \nabla \tilde{h})] + \nabla q_h + Q_{rad} + S_{\rho h}, \quad (6)$$

$$\frac{\partial \bar{\rho} \tilde{Z}}{\partial t} + \nabla \cdot (\bar{\rho} \tilde{\mathbf{u}} \tilde{Z}) = \nabla \cdot [\bar{\rho} (\tilde{D}_Z \nabla \tilde{Z})] + \nabla q_Z + S_{\rho Z}, \quad (7)$$

$$\frac{\partial \bar{\rho} \tilde{C}}{\partial t} + \nabla \cdot (\bar{\rho} \tilde{\mathbf{u}} \tilde{C}) = \nabla \cdot [\bar{\rho} (\tilde{D}_C \nabla \tilde{C})] + \nabla q_C + \tilde{\rho} \tilde{\omega}_C, \quad (8)$$

where, the overbar, $\bar{\cdot}$, denotes the filtered mean value, and the tilde, $\tilde{\cdot}$, denotes the Favre averaged value. $\tau_{sgs} = \bar{\rho}(\tilde{\mathbf{u}}\tilde{\mathbf{u}} - \tilde{\mathbf{u}}\tilde{\mathbf{u}})$ is the subgrid term of the stress tensor, h the enthalpy, Z the mixture fraction. The mixture fraction is defined as the mass fraction of fuel stream, such that $Z = 1$ means a fuel stream and $Z = 0$ means an oxidizer stream. Following the work [52,57], the progress variable C is defined as the summation of combustion products, i.e., $C = Y_{H_2O} + Y_{H_2} + Y_{CO_2} + Y_{CO}$. Y is the mass fraction of chemical species. D_h , D_Z , and D_C are diffusion coefficients of h , Z , and C , respectively. D_h is the gaseous thermal diffusivity given by $D_h = \lambda/(\rho c_p)$, D_Z and D_C are obtained by assuming the unity Lewis number. λ is the heat conductivity, c_p is the specific heat capacity at constant pressure. q_h , q_Z , and q_C are the subgrid-scale (SGS) scalar fluxes, $q_\phi = \bar{\rho}(\tilde{\mathbf{u}}\tilde{\phi} - \tilde{\mathbf{u}}\phi)$, ($\phi = h, Z, C$). Q_{rad} is the radiation heat loss modeled by the weighted sum of gray gases (WSGG) model [58]. $\tilde{\omega}_C$ is the source term of reaction progress variable. The eddy viscosity approximation is used to determine the τ and q as follows,

$$\tilde{\boldsymbol{\tau}}_{sgs} = \mu_t [(\nabla \tilde{\mathbf{u}}) + (\nabla \tilde{\mathbf{u}})^T], \quad (9)$$

$$q_\phi = \bar{\rho} \alpha_t \nabla \tilde{\phi}, \quad (10)$$

where, μ_t and α_t denote the turbulent viscosity and eddy diffusivity, respectively, and are generally related in the formulation as $\alpha_t = \mu_t / (\bar{\rho} Sc)$ with a constant Schmidt number of $Sc = 0.4$ [59], where μ_t is determined by the dynamic Smagorinsky–Lilly model [60].

A non-adiabatic flamelet/progress variable approach (FPV), which can consider the effect of the heat loss caused by the latent heat of spray vaporization and radiation, is used. In order to generate the flamelet library, the following flamelet equations depending on the unity Lewis number assumption with heat loss are solved as follows,

$$\rho \frac{\partial Y_k}{\partial t} - \frac{\rho \chi}{2} \frac{\partial^2 Y_k}{\partial Z^2} - \dot{\omega}_k = 0, \quad (11)$$

$$\rho \frac{\partial T}{\partial t} - \frac{\rho \chi}{2} \left(\frac{\partial^2 T}{\partial Z^2} + \frac{1}{c_p} \frac{\partial c_p \partial T}{\partial Z} \right) + \sum_k \frac{\rho \chi}{2} \left(\frac{\partial Y_k}{\partial Z} + \frac{Y_k}{W} \frac{\partial W}{\partial Z} \right) \left(1 - \frac{c_{p,k}}{c_p} \right) \frac{\partial T}{\partial Z} + \frac{1}{c_p} \sum_k h_k \dot{\omega}_k + q'_{loss} = 0, \quad (12)$$

$$q'_{loss} = -\frac{\alpha}{c_p} \sum_k h_k \dot{\omega}_k, \quad (13)$$

where, the subscript k denotes the chemical species, χ is the scalar dissipation rate, $\dot{\omega}_k$ the reaction rate of species k , T the gas temperature, W the mean molecular weight of mixture, $c_{p,k}$ the specific heat capacity of species k at constant pressure, q'_{loss} the heat loss, α the heat loss rate parameter which can be varied from 0 to 1. Then a four dimensional flamelet library is obtained as,

$$\tilde{\varphi} = \tilde{\varphi}(\tilde{Z}, \tilde{Z}'^2, \tilde{C}, \tilde{\Delta}h), \quad (14)$$

where, Z'^2 is the variance of mixture fraction, Δh is the enthalpy defect due to heat loss, φ is the flame properties such as gas temperature, species mass fraction, and reaction rate. Here, the adiabatic enthalpy h_a is calculated by Eq. (16) by assuming $\Delta h = 0$, i.e., $h_a = \tilde{h}(\tilde{Z}, \tilde{Z}'^2, \tilde{C}, \Delta h = 0)$, and thus the enthalpy defect Δh can be calculated by $\Delta h = h_a - h$, where h is determined with Eq. (6).

The influence of the evaporating droplets on the carrier gas flow is considered using the Particle-Source-In Cell (PSI-Cell) method [61]. S_ρ , $S_{\rho u}$, $S_{\rho h}$, and $S_{\rho z}$, which are the source terms for the mass, momentum, enthalpy, and mixture fraction originating from the dispersed droplets, respectively, are given as follows,

$$S_\rho = -\frac{1}{\Delta V} \sum_N \frac{dm_d}{dt}, \quad (15)$$

$$S_{\rho u} = -\frac{1}{\Delta V} \sum_N \frac{dm_d \mathbf{u}_d}{dt}, \quad (16)$$

$$S_{\rho h} = -\frac{1}{\Delta V} \sum_N \frac{dm_d h_d}{dt}, \quad (17)$$

$$S_{\rho z} = -\frac{1}{\Delta V} \sum_N \frac{dm_d}{dt} \quad \text{for fuel}, \quad (18)$$

where, ΔV is the volume of the unit grid, N is the number of droplets in the grid, and m_d , \mathbf{u}_d , and h_d are the mass, velocity, and specific enthalpy of the droplet, respectively.

Considering the non-equilibrium Langmuir–Knudsen evaporation model [24,62], the governing equations used to track the droplet profiles such as the position, x_d , velocity, \mathbf{u}_d , temperature, T_d , and mass, m_d , are given,

$$\frac{dx_d}{dt} = \mathbf{u}_d, \quad (19)$$

$$\frac{d\mathbf{u}_d}{dt} = \frac{f_1}{\tau_d} (\tilde{\mathbf{u}} - \mathbf{u}_d), \quad (20)$$

$$\frac{dT_d}{dt} = \frac{Nu}{3Pr} \left(\frac{\tilde{c}_p}{c_{p,d}} \right) \left(\frac{f_2}{\tau_d} \right) (\tilde{T} - T_d) + \frac{1}{m_d} \left(\frac{dm_d}{dt} \right) \frac{L_V}{c_{p,d}}, \quad (21)$$

$$\frac{dm_d}{dt} = -\frac{Sh}{3Sc} \frac{m_d}{\tau_d} \ln(1 + B_M), \quad (22)$$

Here, f_1 and f_2 are the correction coefficients for the Stokes drag and heat transfer for the evaporating fuel droplet, τ_d is the particle response time [13,63], T the gas temperature, L_V the latent heat of evaporation at T_d , c_p and $c_{p,d}$ the specific heat of gas and fuel droplet, the Nusselt number and Prandtl number $Nu = 2 + 0.522 Re_{sl}^{1/2} Pr^{1/3}$ and $Pr = \mu c_p / \lambda$, the Sherwood number and Schmidt number $Sh = 2 + 0.552 Re_{sl}^{1/2} Sc^{1/3}$ and $Sc = \mu / (\rho D_k)$, the mass transfer number $B_M = (Y_{F,s} - Y_F) / (1 - Y_{F,s})$. The detailed information of the droplet evaporation model can be found in our previous studies [24,46,64,65]. The employed secondary breakup model is the Taylor analogy breakup (TAB) model [66].

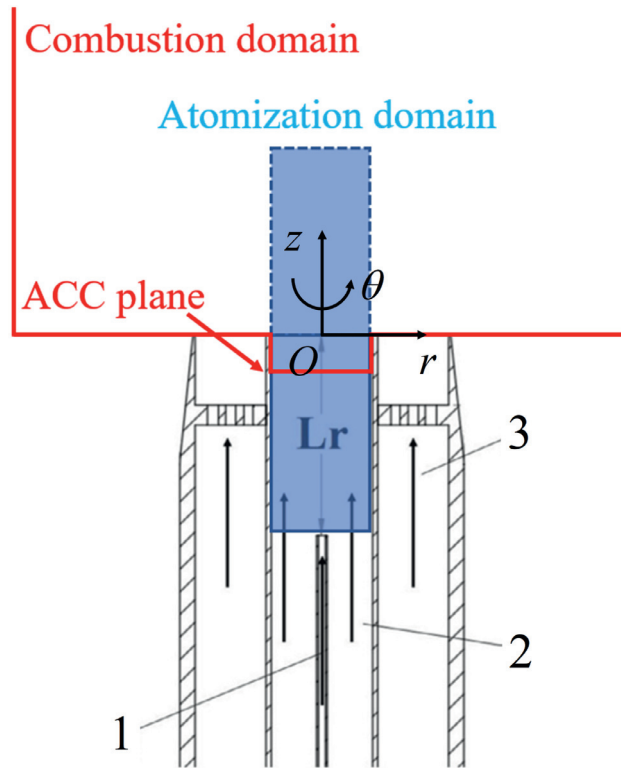
3. Computational setup

3.1. Computational domains

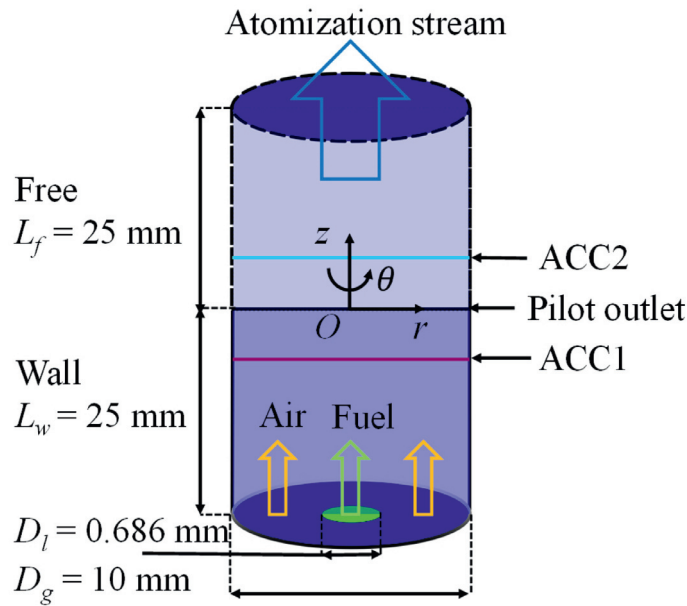
A numerical framework is proposed in the present study, where the spray atomization and the subsequent combustion are simulated using different methods following an assumption that these two sub-processes usually occur in separated domains. Therefore, two computational domains are adopted and are marked as atomization and combustion domains, respectively, as shown in Fig. 1. In Fig. 1(a), the part depicted by the black line is the Sydney Burner, which consists of two concentric tubes, 1 and 2, surrounded by a pilot tube, 3. The inner tube, 1, is the liquid fuel nozzle with an inner diameter of $D_l = 0.686$ mm and wall thickness of 0.381 mm, and the outer tube, 2, is the air stream nozzle for the liquid fuel atomization with an inner diameter of $D_g = 10$ mm and wall thickness of 0.5 mm. The pilot tube, 3, is used to supply the hot combustion products through an inner diameter of $D_p = 25$ mm and wall thickness of 0.2 mm. The concentric tubes are adjustable such that the distance from the liquid fuel nozzle to the pilot outlet is variable, enabling the Sydney Burner to supply a dense or dilute spray for the combustion. The distance is called the recess distance and is referred to as Lr in the present and related studies [e.g., 48,49,50], ranging from 0 to 80 mm. The present study selected two different flame cases, N-AF8-25 and N-AF8-80 which hold different Lr values, $Lr = 25$ and 80 mm, respectively.

However, for the atomization computation, the case of $Lr = 80$ mm requires a much higher computational cost than that of $Lr = 25$ mm. Therefore, only the N-AF8-25 case atomization process is calculated, which is depicted by the solid and dotted blue lines in Fig. 1(a), and is shown in Fig. 1(b) in detail. The atomization domain consists of a region with a wall boundary having a length of 25 mm corresponding to the experimental recess distance and a free boundary of 25 mm. Two atomization-combustion coupling (ACC) planes are set in the atomization domain. These are utilized to transform the Eulerian components into the Lagrangian droplets and serve as the inlet boundary conditions for the combustion simulation. To investigate the influence of different ACC positions on the E-L transformation, one plane is set at 5 mm upstream of the pilot outlet (ACC1) and the other is 5 mm downstream of the pilot outlet (ACC2).

The combustion domain is depicted by the red line in Fig. 1(a), the details of which are presented in Fig. 1(c). The entire combustion domain holds a diameter of $D_c = 104$ mm. In the axial direction, the inlet boundary is placed at the ACC plane, whose distance

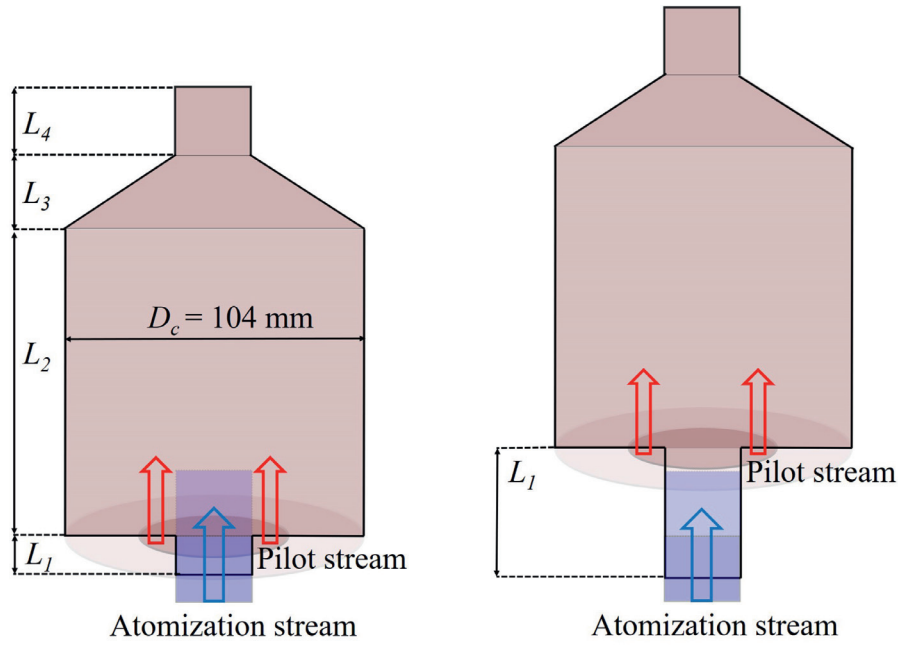


(a) Computational domains of atomization and combustion. 1, 2, and 3 refer to liquid fuel nozzle, air stream nozzle, and pilot tube, respectively and ACC refers to atomization-combustion coupling plane



(b) Computational domain of atomization

Fig. 1. Schematics of computational domains.



(c) Computational domains of combustion (left: N-AF8-25; right: N-AF8-80)

Fig. 1. Continued

to the pilot outlet is marked as L_1 . Since the recess distance of N-AF8-25 and N-AF8-80 are adjusted to 25 and 80 mm to produce dense and dilute sprays, L_1 holds two values of 10 and 65 mm for N-AF8-25 and N-AF8-80, respectively, and the other parameters $L_2 = 1000$ mm, $L_3 = 75$ mm, and $L_4 = 135$ mm are kept the same in both cases.

The cylindrical coordinate system with the unstructured grids is utilized for both atomization and combustion simulations. The atomization computational domain has a total of 24.6 million grid points, with a non-uniform mesh size ranging from 8 to 100 μm in the radial direction, and a uniform mesh size of 100 μm in the axial direction. The combustion computational domain has a total of 18 million grid points, with an increasing mesh size of 0.13 to 3 mm in the radial direction, and a variable mesh size of 0.15 to 3.5 mm in the axial direction. In addition, the Hinze scale $\eta_H = \sigma / (\rho_g U_g^2)$ in the atomization computation is estimated to be 8.54 μm and the mesh size holds 1–10 η_H . As suggested in our previous study [46] and regarding this simulation reaches to the experimental scale, it could be considered as a high-resolution VOF simulation.

3.2. Computational conditions

For the atomization computation, the temperature and pressure are set to room temperature and atmospheric pressure, and hence, both the liquid fuel and air have a temperature of 300 K, which can be regarded as a cold state for only atomization, neglecting the evaporation effect. Therefore, the air viscosity, μ_g , is 1.81×10^{-5} Pa s, and liquid viscosity, μ_l , is 3.33×10^{-4} Pa s, the liquid-gas surface tension, σ , is 2.37×10^{-2} N/m. At the inlet, both the liquid and carrier gas velocities, u_l and u_g , are assigned as 2.57 m/s and 48 m/s with a flat laminar velocity profile, respectively, according to the experiments [49,50]. Thus, in both configurations, i.e., N-AF8-25 and N-AF8-80, the dimensionless parameters, including the aerodynamic Weber number, $We = \rho_g u_g^2 D_l / \sigma$, evaluated as 80, the liquid jet Reynolds number, $Re_l = 4161$, as well as the carrier gas Reynolds number, $Re_g = 31,823$, are close to the

Table 1

Parameters for atomization simulation.

Physical properties	
Liquid fuel	Acetone
Gas&Air	
Liquid nozzle diameter, D_l (mm)	0.686
Liquid jet velocity, u_l (m/s)	2.57
Liquid jet viscosity, μ_l (Pa s)	3.33×10^{-4}
Liquid jet density, ρ_l (kg/m ³)	786
Liquid jet temperature, T_l (K)	300
Liquid jet Reynolds number, Re_l (-)	4161
Gas jet diameter, D_g (mm)	10
Gas jet velocity, u_g (m/s)	48
Gas jet viscosity, μ_g (Pa s)	1.81×10^{-5}
Gas jet density, ρ_g (kg/m ³)	1.20
Gas jet temperature, T_g (K)	300
Gas jet Reynolds number, Re_g (-)	31,823
Liquid-gas surface tension, σ (N/m)	2.37×10^{-2}
Ambient pressure, P (MPa)	0.1
Aerodynamic Weber number, We (-)	80

experimental conditions, as shown in Thomas and Lowe's works [49,50]. The parameters used in the atomization computation are shown in Table 1.

After the atomization computation, the droplets are transformed into the Lagrangian droplets, which are stored in a database for the following combustion computation. Droplets recorded at the ACC plane of the atomization domain are directly injected into the combustion domain at the ACC plane at a fixed time step determined by satisfying the step interval of the combustion computation, which are explained in the following section. When these cold Lagrangian fuel droplets flow out of the nozzle and face the hot pilot gases, combustion occurs after the evaporation and mixing with the combustion products from the pilot that is in the stoichiometric condition and has a velocity of 1.5 m/s. Two different gas velocity profiles: (1) a uniform flat gas velocity that equals to 48 m/s; (2) a gas velocity profile extracted from the

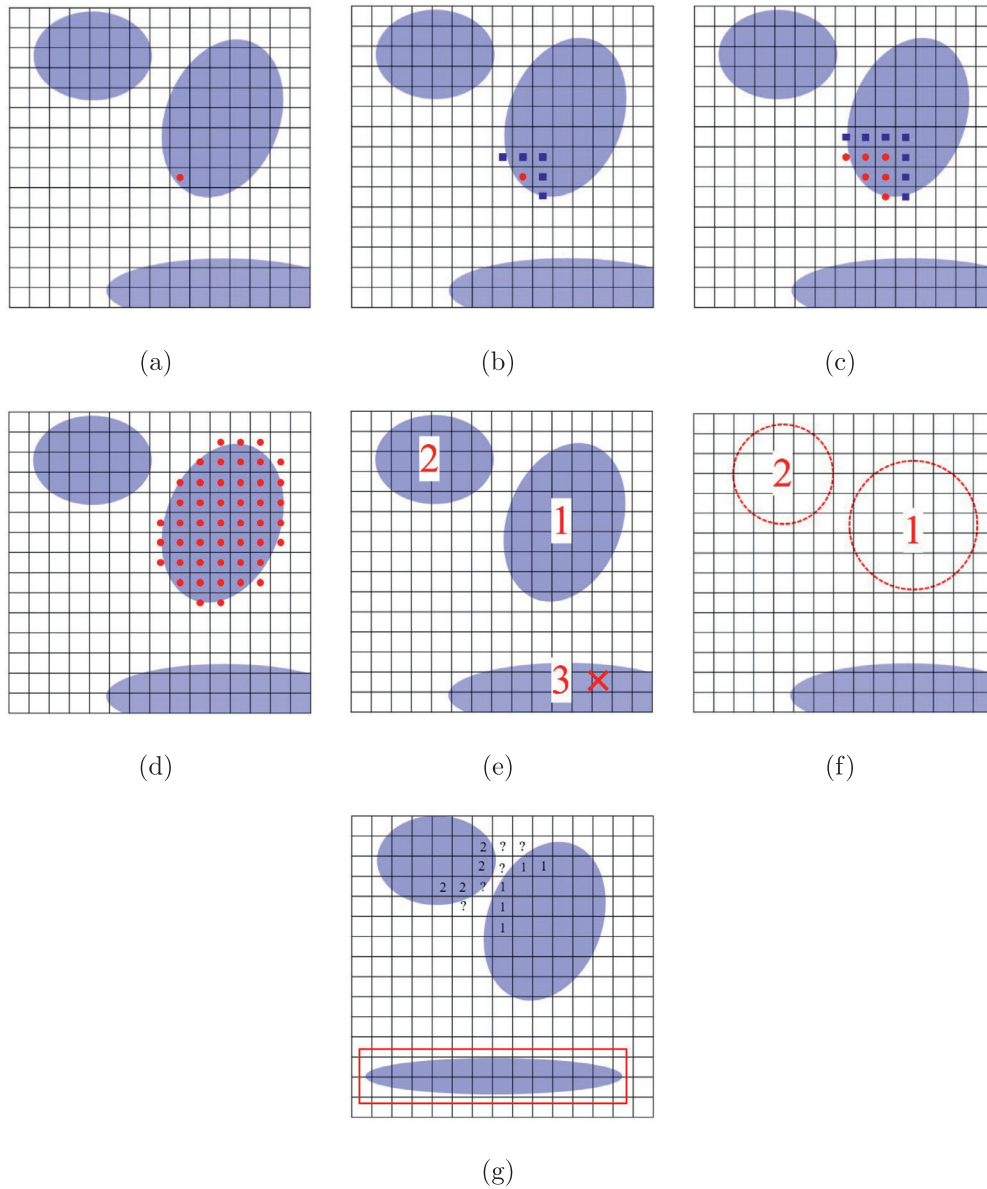


Fig. 2. Algorithm of E-L tagging method.

atomization computation, are performed to study the influence of different inlet gas velocity profiles.

The flamelet calculations for the flamelet library generation are conducted with FlameMaster code [67]. The numbers of grids set for \tilde{Z} , $\tilde{Z}^{1/2}$, \tilde{C} , and $\tilde{\Delta}h$ are $100 \times 20 \times 100 \times 10$. The reaction mechanism for acetone/air combustion proposed by Pichon et al. [68] is employed, which consists of 81 species and 416 reactions.

The computational cost for single realization of atomization and combustion simulations, performed on the Kyoto University Supercomputer (Cray XC40), are around 430k core-hours (840 h in real time using 512 cores) and 250–370k core-hours (230–340 h in real time using 1088 cores), respectively.

4. Results and discussion

4.1. Atomization and E-L transformation

In the experiments of the dense sprays, it is difficult to acquire confident droplet size distribution owing to the diagnostics limita-

tion. In fact, Lowe et al. [50] reported that large numbers of ligaments and irregular shaped objects are formed before secondary breakup. Those ligaments and irregular shaped objects are considered to more likely increase the turbulence in the flow field. Although such liquid ligaments and irregular shaped objects are also observed in the present simulation, those are forced to be transformed into Lagrangian sphere droplets using a E-L tagging method owing to the limitation of the consideration of those shapes. The influence of this will be discussed later.

The E-L tagging method is used to recognize the dispersed Eulerian components generated by the primary breakup during the atomization process and transfer their properties into the Lagrangian droplets, which are later directly placed in the computational domain to replace the Eulerian components. To simply explain the E-L tagging method employed in the present study, 2-dimensional schematics are given as shown in Fig. 2. First, a threshold for the tagging method should be artificially given, with which the cells satisfying the criterion would be tagged and then become one part of a transformed Lagrangian droplet. In the present study, the

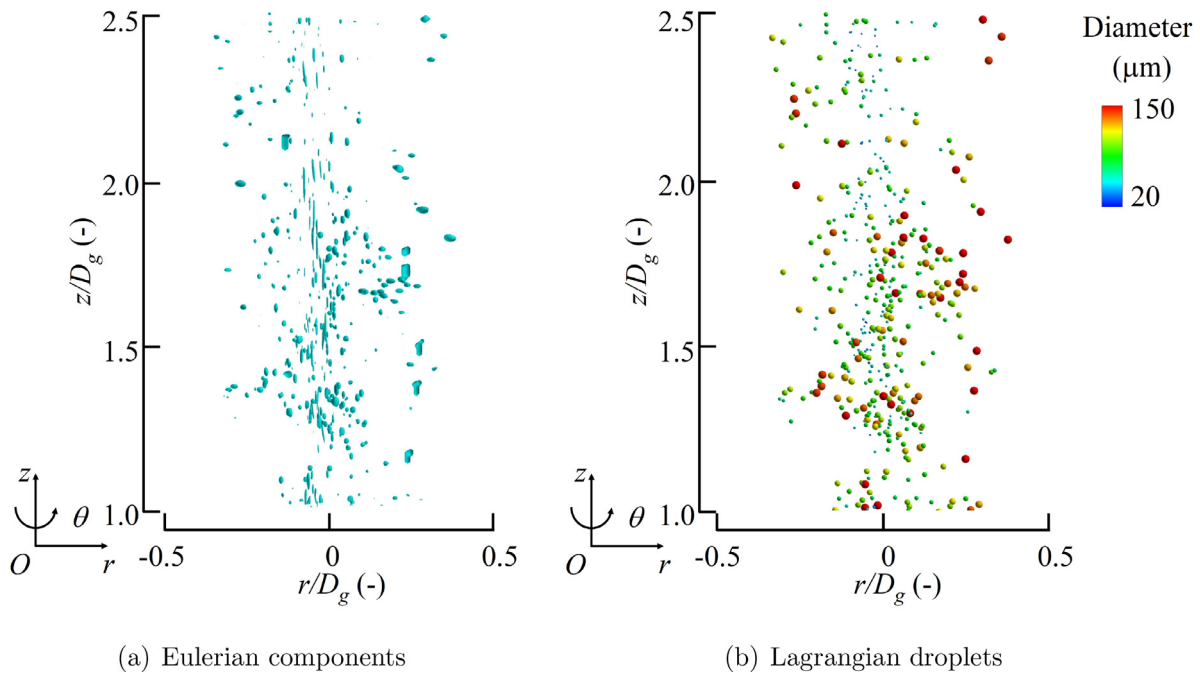


Fig. 3. Comparison of droplet position and size distributions between Eulerian components and Lagrangian droplets at $1.0 \leq z/D_g \leq 2.5$ and $-0.5 \leq r/D_g \leq 0.5$ (Lagrangian droplets are colored and scaled by diameter size).

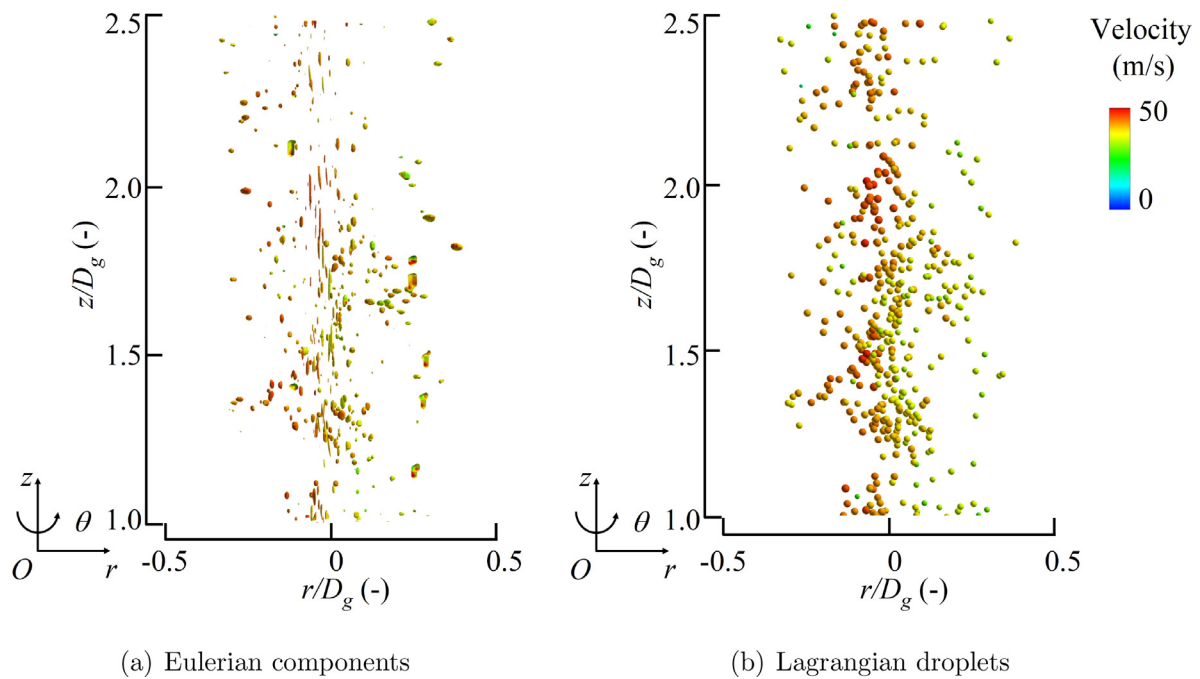


Fig. 4. Comparison of axial velocity and position distributions between Eulerian components and Lagrangian droplets at $1.0 \leq z/D_g \leq 2.5$ and $-0.5 \leq r/D_g \leq 0.5$ (Eulerian components and Lagrangian droplets are colored by velocity).

volume fraction of gas phase $VOID = 1 - \psi$, is used for the tagging method, and hence the threshold for the $VOID$ value is set as $VOID_{cri}$.

For a cell satisfying $VOID < VOID_{cri}$, it would be tagged by a red marker as shown in Fig. 2(a). The surrounding cells are then checked and also the cells satisfying $VOID < VOID_{cri}$ are tagged by blue markers, which represent the edge of the tagged droplet as shown in Fig. 2(b). Later on, the cells neighboring the edge of the tagged droplet are checked and tagged by blue markers to represent the new edge of the tagged droplet, and the original blue

markers are switched to red markers to represent the inside of the tagged droplet as shown in Fig. 2(c). By looping the steps from (b) to (c), a droplet would be filled by red markers and no further neighboring cells could be tagged by blue markers, then all markers are switched to red markers as shown in Fig. 2(d), which would later be tagged by a specific marker such as 1 shown in Fig. 2(e). By employing the steps from (a) to (d), all the dispersed Eulerian components would be tagged by the specific markers such as 1, 2, and 3, as shown in Fig. 2(e). Then the details of each tagged Eulerian component would be further checked. For example, for 3 in

Fig. 2(e), some cells in it are neighboring the wall boundary such that the detailed information could not be further checked, which makes 3 unable to be recognized as a Lagrangian droplet as shown in Fig. 2(f). Some more complex situations are provided in Fig. 2(g), for example, how to deal with the cells marked by the question marks since they should belong to two individual droplets, or how to deal with the dispersed component with extremely slim structure marked by the red rectangle. Therefore, for more interests of this tagging method, please refer to the work of Herrmann [56], Zuzio et al. [69] as well as our previous work [46].

In the present study, the E-L transformation is triggered only if the Eulerian droplet passes through the ACC plane, as shown in Fig. 1(b), which is a cross-section at the downstream region in the atomization computational domain. Therefore, a buffer region is created upstream of the ACC plane, and the Eulerian components in this buffer region that can pass through the ACC plane within one sampling time interval are transformed into Lagrangian droplets and then saved in the database for subsequent combustion. Because the computational time interval used for the combustion simulation is 1×10^{-5} s, and that for the atomization simulation is 5×10^{-8} s, the sampling time interval is thus set as 200 steps of the atomization computation, that is, 1 step of the combustion simulation.

Figures 3 and 4 show comparisons of the position, size, and axial velocity between the Eulerian components and the transformed Lagrangian droplets. Generally, a good agreement is observed. Specifically, it can be seen that the Lagrangian droplets with a red color match the large Eulerian components in both the droplet position and size. A good match is also shown for the small droplets with a green color. Such an agreement of the axial velocity profiles can also be found in Fig. 4. Therefore, the present E-L tagging method can work properly to transform Eulerian components into the Lagrangian droplets.

4.2. Atomized droplets database

4.2.1. Database concept and droplet size distribution

To confidently build a database serving as the inlet boundary conditions for the combustion computation, the critical factors affecting the atomization properties should be carefully checked. The present E-L tagging method includes three important parameters, i.e., the downstream distance from the fuel nozzle to the ACC plane, Z_0 , the threshold value of the E-L tagging method, and the total sampling time for recording the droplets profiles. Regarding the downstream distance Z_0 , with a smaller Z_0 , where the liquid jet is not fully developed, the E-L tagging method cannot transform the ligaments and irregular shaped objects into larger Lagrangian blobs, which is unrealistic, resulting in mass loss; however, with a larger Z_0 , where less ligaments exist and Eulerian droplets are easily transformed into the Lagrangian droplets, the E-L tagging method also loses its accuracy owing to the numerical diffusion since the cells might hold diffused VOF values and the unexpected transformed Lagrangian droplets. Therefore, two different ACCs, i.e., one is 5 mm upstream of the pilot outlet (ACC1) and another is 5 mm downstream of the pilot outlet (ACC2), which are shown in Fig. 1(b), are exhibited to check the confidence of the position. On the other hand, considering the threshold values used in the E-L tagging method, a larger threshold, which can recognize the tiny Eulerian droplets, increases the risk of numerical error caused by numerical diffusion, some of which are simply numerical noise and referred to as fake droplets. However, a smaller threshold neglects those droplets with a small scale in comparison to the local grid size, losing realistic small droplets, which have a significant influence on the subsequent evaporation and combustion properties. Thus, three different thresholds, $VOID_{crit} = 0.9, 0.95,$ and 0.99 , are selected and their validities are examined. Hence, four different

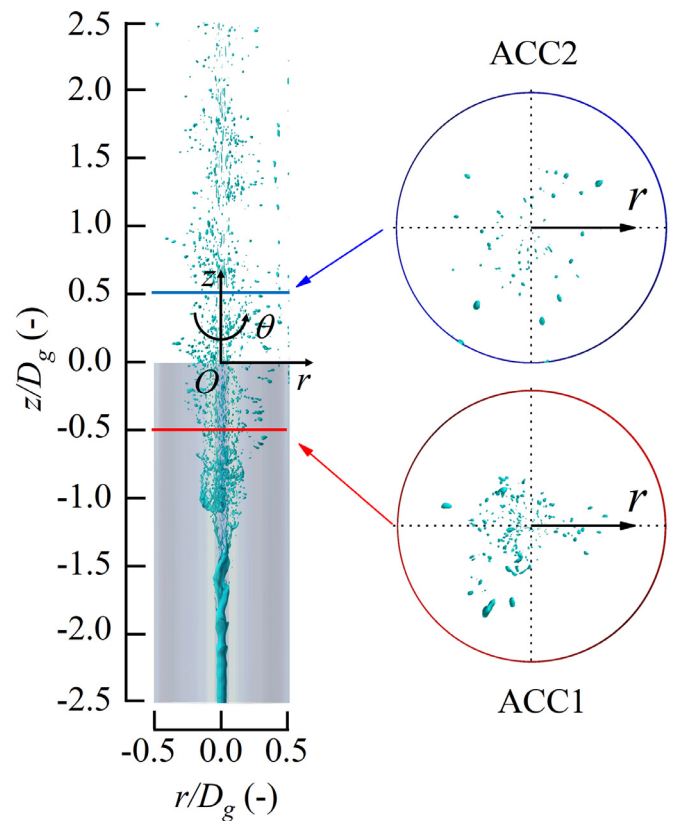


Fig. 5. Atomization behavior and the Eulerian components distributions at ACC1 and ACC2 ($VOID_{crit} = 0.9$).

databases can be acquired, as presented in Table 2. Note that the atomization simulation is only calculated once under the condition shown in Table 1, and the droplet databases are obtained during the simulation by setting different ACCs and thresholds.

Figure 5 shows the atomization behavior in the front view and at the cross-sections of ACC1 and ACC2, the colored surface of which is the iso-surface of the E-L tagging method threshold of 0.9, i.e., the liquid-phase volume fraction of the grids is larger than 10%. The liquid column starts to show instability around the downstream at $z/D_g = -2.25$, and twists at approximately $z/D_g = -1.75$. When it passes $z/D_g = -1.5$, a breakup behavior can be observed. The liquid column becomes discontinuous, and smaller droplets and some ligaments and irregular shaped objects can be found around the $z/D_g = -1.0$. Beyond $z/D_g = -0.5$, most of the visible liquid phase is due to dispersed droplets, which tend to flow away from the center axis. By comparing the cross-sections of ACC1 and ACC2, the existing droplets are found to be denser at ACC1, and the downstream droplets at ACC2 reach further in the radial direction.

Figure 6 shows the droplet profiles in different databases, plotted with droplet diameters which are binned over 10 μm interval for droplets up to 50 μm , 20 μm interval for droplets from 50 to 150 μm , and 50 μm interval for droplets with size above 150 μm . For Fig. 6(a), with the ACC plane going downstream and increasing the threshold of the E-L tagging method, the peak of the PDF value changes from 70 to 30 μm . By comparing the droplet size distributions of A1 and A2 in three different clusters, i.e., 0–50 μm , 50–150 μm , and 150–200 μm , there are few differences between both cases, indicating occurrences of further breakup. Moreover, the threshold of the E-L tagging method seems to have a more significant influence on the droplet size distribution than the ACC position by comparing the differences between A2 and A4 as well as A1 and A2. By applying a larger threshold, more droplets with the

Table 2
Databases acquired in atomization simulation.

Database	ACC plane	Threshold for E-L transformation	Volumetric particle loading
A1	ACC1	0.9	7.40
A2	ACC2	0.9	9.28
A3	ACC2	0.95	9.84
A4	ACC2	0.99	11.22

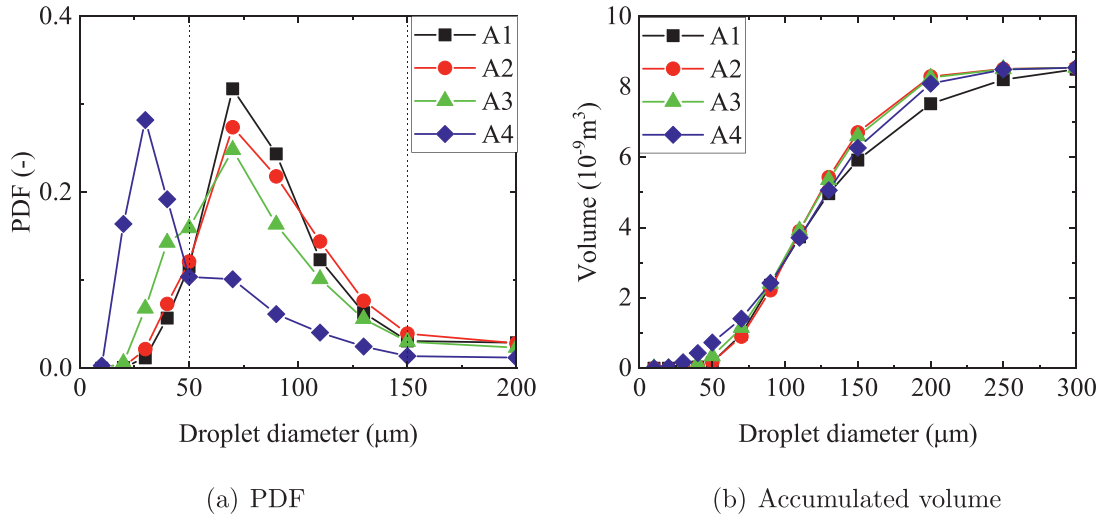


Fig. 6. Droplet size distribution in terms of (a) PDF and (b) accumulated volume of different atomization databases (A1–A4).

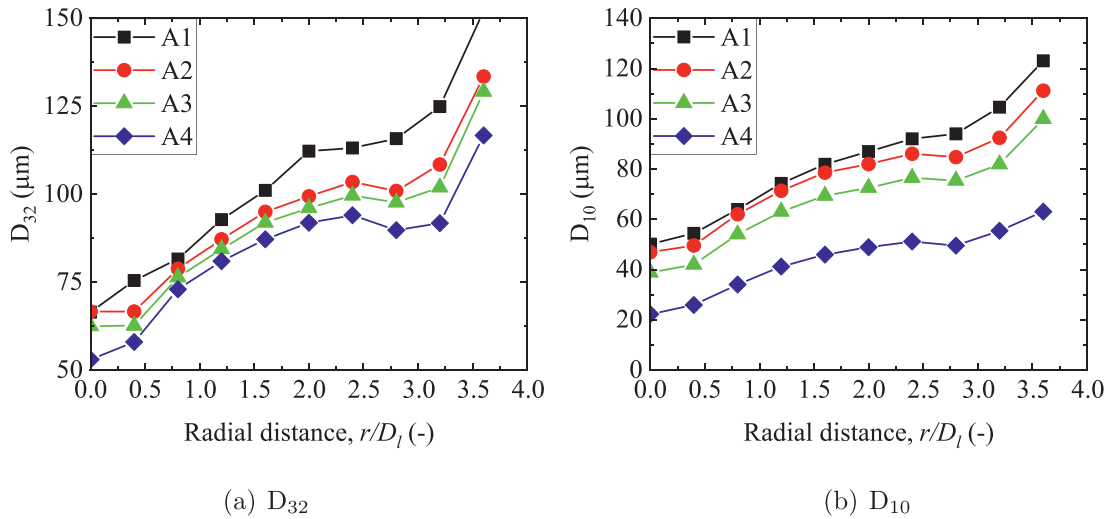


Fig. 7. Radial distributions of droplet size in (a) D_{32} and (b) D_{10} for different atomization databases (A1–A4).

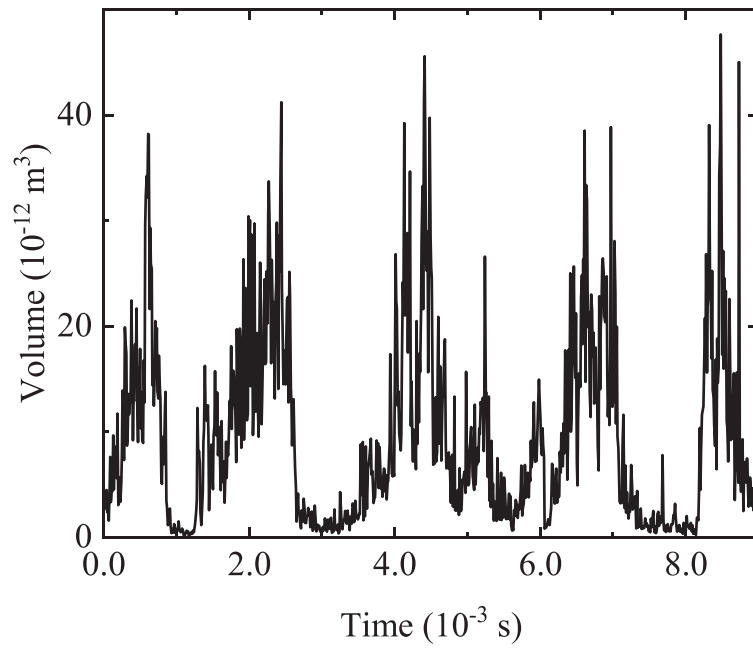
diameter less than 50 μm seem to be captured with the value of 0.99. By comparing the total droplet volume of different databases shown in Fig. 6(b), all databases show a similar total droplet mass, which means that almost of the Eulerian components are captured by the present E-L tagging method. In addition, one thing worth noting is that for a large Lagrangian droplet, which might be comparable to the mesh size, the mass and momentum interactions between gas phase and the Lagrangian droplet are decided by the surrounding cells instead of the local cell such that the Lagrangian droplet could be still considered as a point by the PSI-Cell method.

Because this study is focused on dense spray, the volumetric particle loading of droplets in the computational domain is further checked, as shown in Table 2. Here, the ratio of droplet distance and droplet diameter is presented instead of simple volume fraction, which can refer to as S/d in Elghobashi's work [70], where,

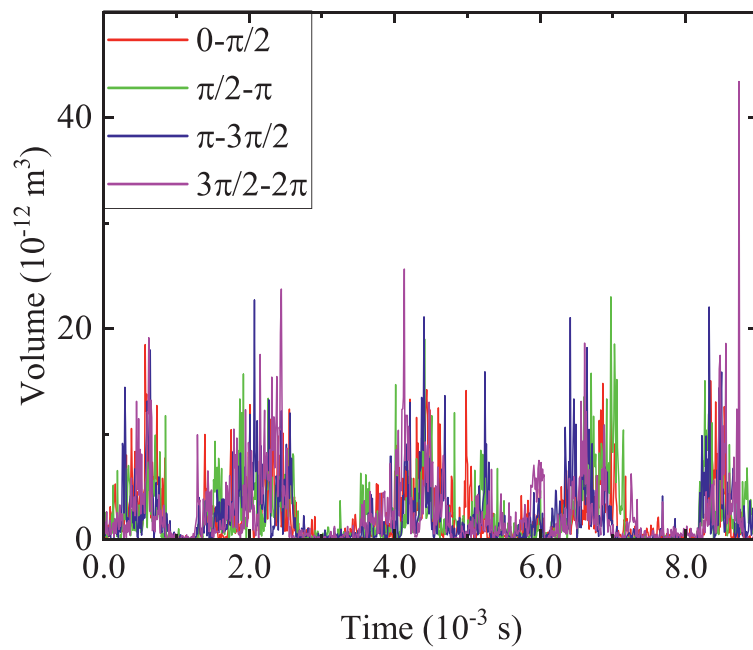
S indicates the distance between the centers of two neighboring droplets, and d denotes the diameter of droplet. With $S/d \geq 10$, the two-way coupling method could be employed in this study instead of four-way coupling. When the ACC plane is set further downstream, the droplets can reach further in the radial direction, which can refer to the cross-sections of ACC1 and ACC2 in Fig. 5, and thus A2 shows a larger value than A1, indicating a more dilute spray compared with A1.

4.2.2. Droplet spatial and temporal size distributions

In traditional combustion simulations, the sizes of droplets issued from the inlet boundary are often given using a simple atomization model or a presumed droplet size distribution. In this study, on the other hand, those are taken from a database resulting from the atomization computation. Therefore, the sampling time of



(a)



(b)

Fig. 8. Time variations of droplet volume through ACC1 plane for the database A1: (a) in total, (b) each quadrant.

atomization computation should be carefully discussed. To obtain a symmetrical flame structure without any preferences in any directions, the spatial distribution of the droplets must be checked such that the position profile should be spatially homogeneous without any biases in any directions. For example, many more larger droplets can be found in $\pi \leq \theta < 3\pi/2$ and fewer droplets can be found in $0 \leq \theta < \pi/2$ at ACC1, and larger droplets are observed on the right side at ACC2, as shown in Fig. 5, thus the droplets distribution shows some preferences if the sampling time is insufficient.

The complexity of the azimuthal homogeneity analysis increases if the droplet size is further considered. Figure 7 shows

the Sauter mean diameter (D_{32}) and arithmetic mean diameter (D_{10}) radial distributions obtained from the different databases. The droplet size for either D_{32} or D_{10} increases as the droplets flow further away from the central axis, which means that the droplet size has a strong correlation with the radial distribution, and thus it is sufficient to base the analysis for azimuthal homogeneity on investigating the droplet size with different angles θ in the radial plane. The droplet size can be used to represent the radial distance between the droplet and the center axis, and the angle θ can be used to represent different radial directions. In addition, referring to the experimental study [50] based on the Sydney Burner

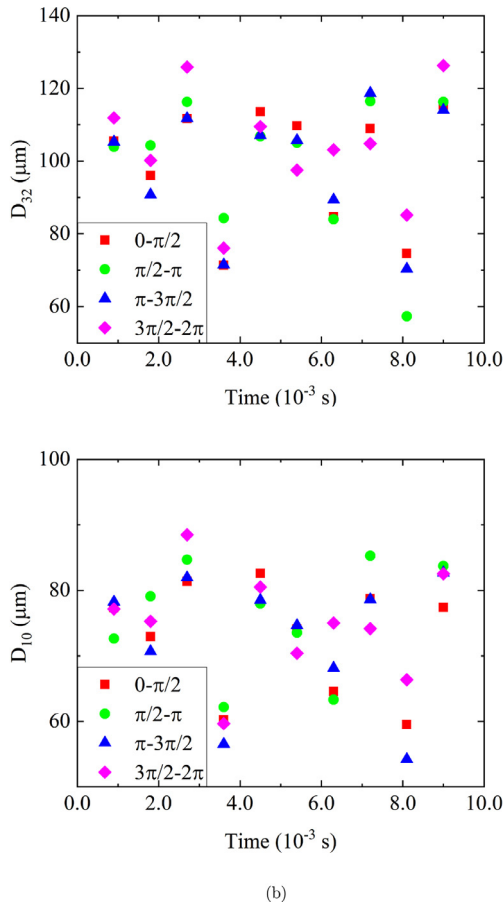


Fig. 9. Time variations of D_{32} and D_{10} of droplets through each quadrant of ACC1 plane for the database A1: (a) D_{32} , (b) D_{10} .

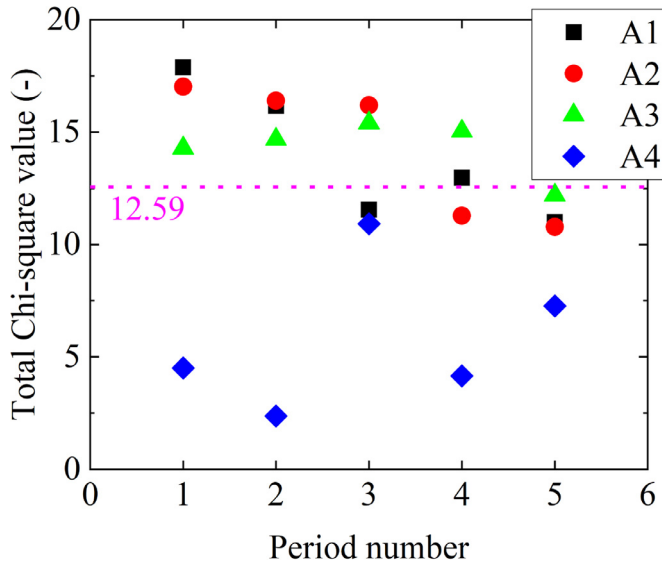


Fig. 10. Total values of different databases A1–A4 with different sampling time.

of N-AF8-25 and N-AF8-80, which only supplies the D_{32} distributions along the center axis (see Fig. 12), D_{32} is always less than $60 \mu\text{m}$. Given that the database of A4 holds the D_{32} value less than $60 \mu\text{m}$, whereas those of other three cases are larger than $60 \mu\text{m}$, the database A4 provides a better droplet size distribution according to the experiment.

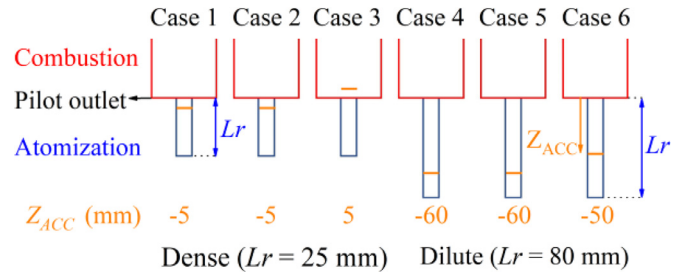


Fig. 11. Conducted cases and schematic of locations of recess distance, L_r , and ACC planes, Z_{ACC} , for combustion in detail.

To obtain a sufficient number of reliable data for a homogeneous analysis, the sampling time and interval are discussed. The sampling interval is set $1 \times 10^{-5} \text{ s}$, which is 200 steps for the atomization computation and 1 step for the combustion computation, and thus the combustion simulation can simply read the data in a step-by-step manner. Figure 8 shows the time variations of droplet volume through ACC1 plane and through each quadrant of ACC1 plane, from the 120,000th step, in which the liquid jet is thought to be fully developed and starts to steadily breakup, to the 300,000th step, which is thought to be long enough for sampling. Five periods can be observed in Fig. 8(a) showing that the atomization process holds a periodic characteristic with breakup and non-breakup periods. In Matas's study [71,72], the frequency of the liquid jet breakup is found to have a strong relation to the gas and liquid velocities as well as the nozzle size, and the empirical correlations are shown as follows.

$$f = \left(\sqrt{\frac{\rho_g \delta_l}{\rho_l \delta_g}} u_g + u_l \right) / D_g, \quad (23)$$

$$\delta = \nu_0 / \max \left(\frac{d\nu}{dr} \right). \quad (24)$$

where δ is the thickness of the vorticity layer, ν denotes the radial velocity, and ν_0 is the radial velocity measured near the Sydney Burner nozzle, e.g., $z/D_g = 0$. The thickness of the vorticity layer of liquid and gas phases, δ_l and δ_g are directly acquired in the simulation. By this correlation, the calculated result is 547 Hz, and the mean period shown in Fig. 8(a) is simply calculated as 556 Hz. Therefore, the present detailed numerical simulation and the E-L tagging method are considered to be reasonable to reproduce the atomization phenomena. Figure 8(b) shows the variations of droplet volume through each quadrant of ACC1 plane, and it could be observed that the droplet volume of each quadrant shows totally different values in different breakup periods. For example, for the quadrant of $3\pi/2 - 2\pi$, it holds larger values in the later time in each breakup period except for the 3rd period between 3 and 5 ms. Figure 9 also shows the time variations of D_{32} and D_{10} through each quadrant of ACC1 plane in each a half breakup period. It could be observed that the values of D_{32} and D_{10} in each a half breakup period are totally different such that the droplet sampling time for acquiring a homogeneous distribution need to be further checked.

By comparing the D_{32} and D_{10} distributions in Fig. 7, the droplet size has a strong correlation with the radial distance, that is, the closer the droplets to the center axis, the smaller the droplets are. Therefore, the angle θ in the radial plane and the droplet size can be used to analyze the droplet spatial distribution by the Chi-square homogeneity check, the detail of which can be found in Appendix A.

Table 3 shows the calculated chi-square values of the database A1 with a sampling time starting at the 120,000th step and ending up with the 300,000th step, covering five full-breakup peri-

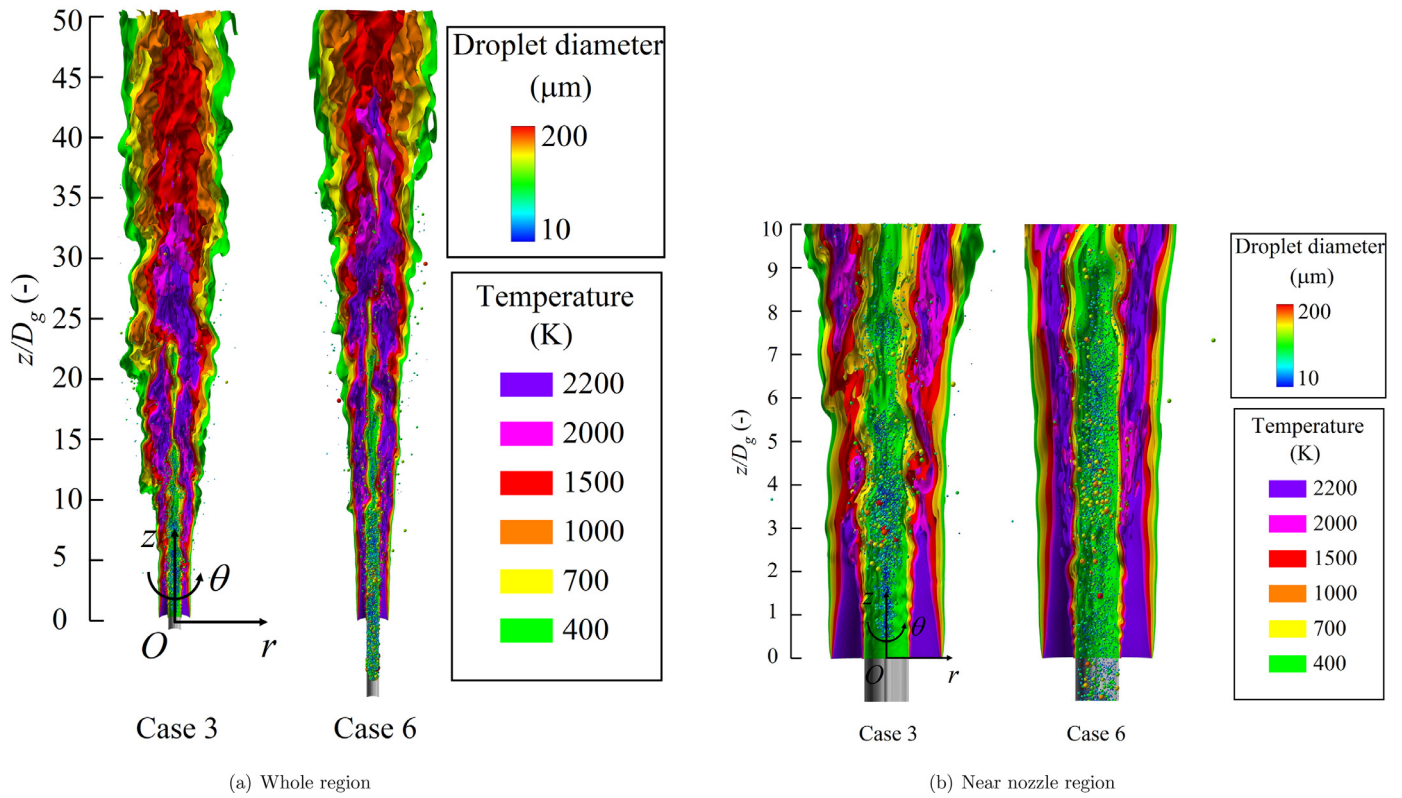


Fig. 12. Instantaneous gas temperature iso-surface and droplet distribution for Cases 3 and 6.

Table 3
Chi-square homogeneity check for the database A1.

A1	$0 - \pi/2$	$\pi/2 - \pi$	$\pi - 3\pi/2$	$3\pi/2 - 2\pi$	Total
0–50 μm	0.12	0.27	4.88	1.77	7.04
50–150 μm	0.11	0.02	0.78	0.16	1.07
150–300 μm	0.56	0.22	0.80	1.32	2.9
Total	0.79	0.51	6.46	3.25	11.01

ods. Compared to other cells, there is an odd value particularly larger than the others, which is marked as red in $\pi \leq \theta < 3\pi/2$ with a diameter of less than 50 μm . It means that in the region $\pi \leq \theta < 3\pi/2$, more droplets with a diameter of less than 50 μm exist compared to the other three regions. Because the number of droplets with diameter of less than 0–50 μm is very small in the database A1 (see Fig. 6(a), black line), it is reasonable to observe such a bias that some region holds a different number of droplets because the droplets generated by the breakup fluctuate spatially and temporally. However, the total value of this case is 11.01, which is less than the critical value of 12.59, ensuring that the spatial distribution of the droplets has no obvious bias by sampling the five breakup periods from the 120,000th step to the 300,000th step.

Figure 10 shows the total values of each database by employing different sampling times from one to five periods. The total values of A1 and A2 continue decreasing when the sampling time is increased from one to five periods, out of which the total values of A4 continue fluctuating because the number of small droplets with a diameter of 0–50 μm of A4 is larger than those of the other three cases, thus those odd values (an example is shown in red in Table 3) are decreased such that the total value is much smaller than those of the other three cases. By sampling five breakup periods, all four databases hold reasonable total values to ensure the azimuthal homogeneity, and the sampling time is thus selected to

be five breakup periods from the 120,000th step to the 300,000th step.

In total, for the atomization computation, the physical time is 15 ms, in which the first 6 ms is used for the liquid jet development to reach a steady state, and the last 9 ms is used for the droplet database sampling discussed in this section. For the combustion computation, the physical time is 100 ms such that the particle injection is cycled about 11 times.

4.3. Combustion characteristics

4.3.1. Simulation cases and flame features

As mentioned in Section 3.1, two different configurations, N-AF8-25 and N-AF8-80, are utilized with representative recess distance of 25 mm and 80 mm. In addition, two different inlet gas velocity profiles, one flat and the other extracted from the atomization computation, are incorporated to study the sensitivity of the dense spray flame to the inlet boundary conditions. Further, considering the computational cost, out of the four databases of A1 to A4 two databases, A1 and A4, are selected to investigate the influence of the droplet inlet boundary conditions on the flame characteristics because A1, A2, and A3 display similar droplet size profiles of D_{32} and D_{10} , whereas A1 holds different gas velocity compared to A2–A4. Therefore, a total of six cases are discussed as shown in Table 4, Fig. 11 provides a clear schematic of the conducted six cases. The orange lines depicted in the figure indicate the ACC planes, where the droplets are recorded in the atomization computation and are applied in the combustion computations as the inlet boundary conditions. In addition, the axial distance of the ACC plane Z_{ACC} relative to the pilot outlet, is displayed for a better understanding.

In dense sprays, laser diagnostic measurements are difficult owing to the co-existence of liquid fragments and abundant atomized droplets, which reflect and absorb the light. Therefore, a chirped-

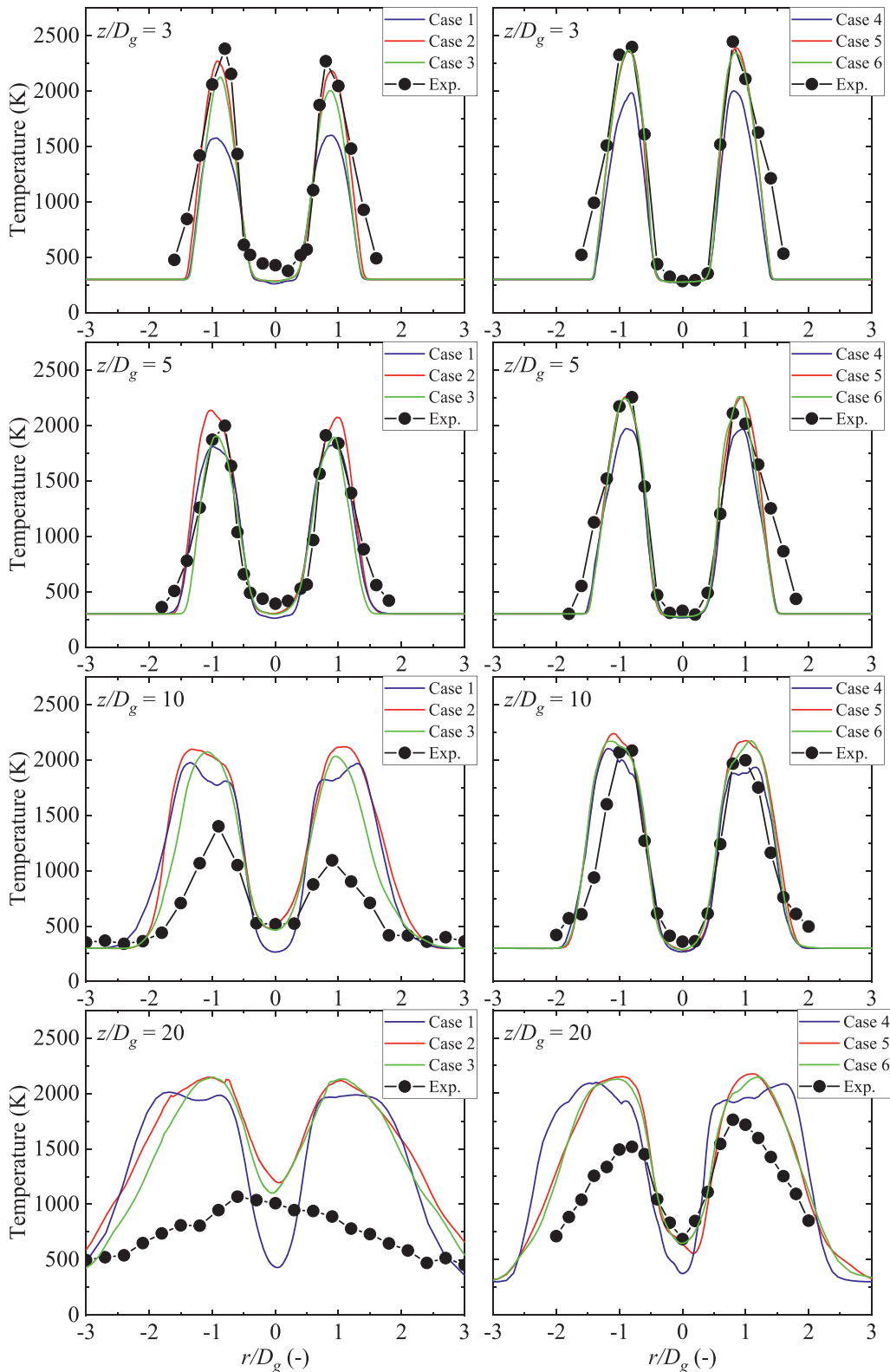


Fig. 13. Comparison of radial distributions of time-averaged of gas temperature at different axial downstream locations of $z/D_g = 3, 5, 10,$ and 20 between combustion simulation and experiment for Cases 1-6. Left is for dense spray and right is for dilute spray.

probe-pulse femtosecond coherent anti-Stokes Raman spectroscopy (CPP-fs-CARS) with a repetition rate of 5 kHz was employed by Thomas and Lowe [49,50] to measure the gas temperature distribution based on the platform of the Sydney Burner, which supplies various gas temperature profiles ranging from dense to dilute

sprays with ethanol and acetone fuels. The gas temperature distributions in both the dense and dilute sprays with the acetone fuel are considered in this work to validate the proposed numerical simulations.

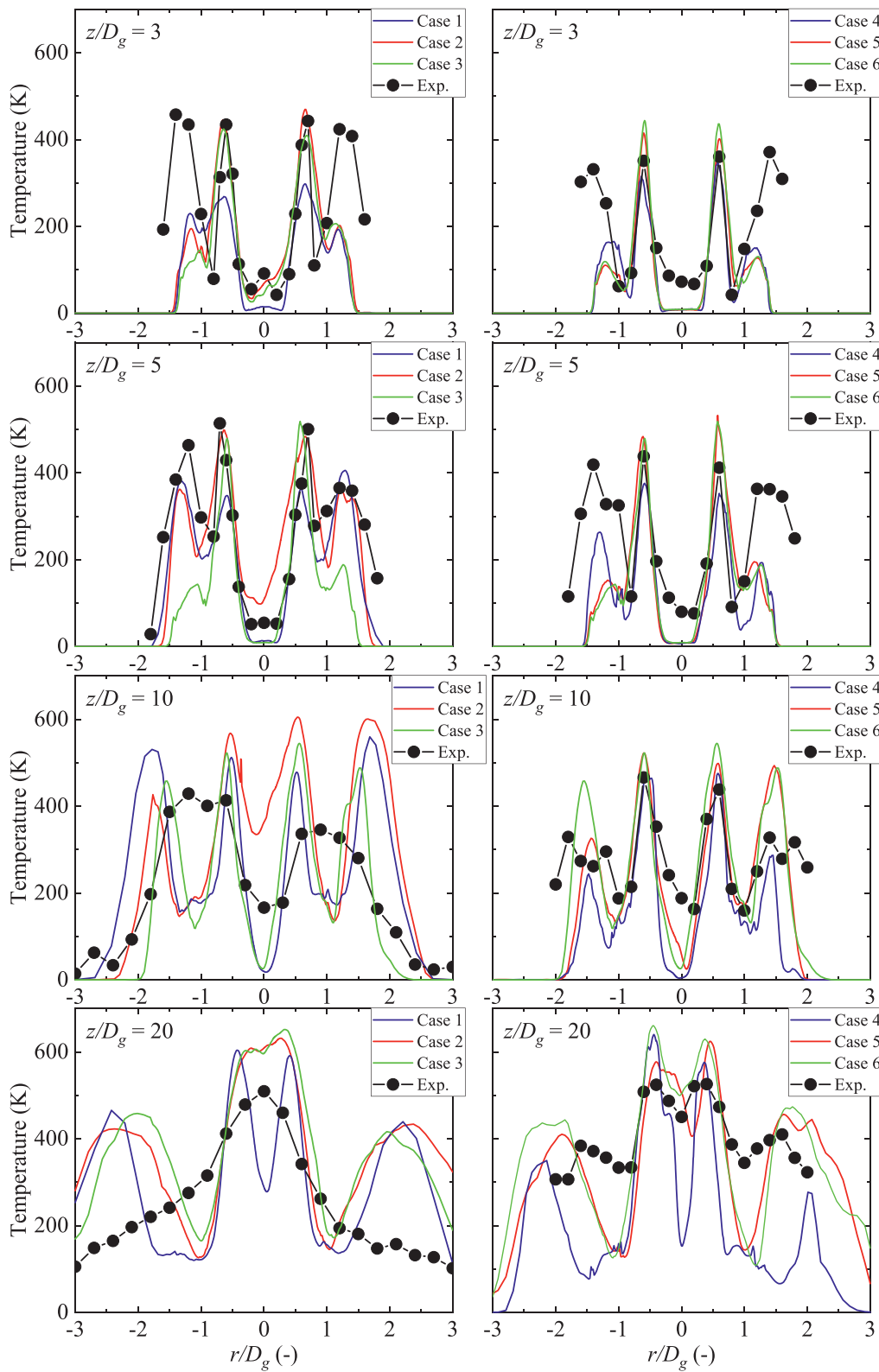


Fig. 14. Comparison of radial distributions of RMS of gas temperature at different axial downstream locations of $z/D_g = 3, 5, 10,$ and 20 between combustion simulation and experiment for Cases 1–6. Left is for dense spray and right is for dilute spray.

Table 4
Conducted cases for combustion simulation.

Case	Velocity profile	Atomization database	Configuration
1	Flat	A1	Dense
2	Atomization	A1	(N-AF8-25)
3	Atomization	A4	
4	Flat	A1	Dilute
5	Atomization	A1	(N-AF8-80)
6	Atomization	A4	

Figure 12 shows the instantaneous gas temperature profiles and fuel droplets distribution for Cases 3 and 6. The double reaction zone, where a premixed core is inside a surrounding non-premixed zone, can be observed. The premixed cores are extended in both the span and axial directions despite the recess distance changes from 25 to 80 mm. Meanwhile, each temperature iso-surface in Case 3 is shorter than that of Case 6, which means that the dilute spray (Case 6) with a longer recess distance can enhance the mixing and combustion processes.

4.3.2. Comparisons with experiments

Figures 13 and 14 show the radial distributions of the time-averaged and RMS of gas temperature at different axial downstream locations, $z/D_g = 3, 5, 10,$ and 20 , where the experimental data are compared with simulations of Cases 1–6 detailed in Table 4. The influences of the inflow gas velocity profiles and inflow droplet profiles are discussed.

The computed results of the mean gas temperature depict a symmetric unimodal distribution at different axial locations, and at the downstream of $z/D_g = 20$, the peak temperature is suppressed. However, based on the experiments at $z/D_g = 20$, the symmetric unimodal distribution is absent for the dense case, and is still distinguished in the dilute case. The reason for this difference is thought to be the result of a higher proportion of fragments and filaments presented in the dense case [49,50], which leads to a less stable and lower mean temperature. By contrast, at the upstream locations of $z/D_g = 3$, the flame is more dominated by the pilot flame such that the reaction zone is less affected by the spray properties and a similar temperature profile is observed for both dense and dilute flame cases. Regarding the simulation results, the atomization velocity presents its priority in comparison to the flat one, showing a good agreement with experiments at the upstream region. Even for the $z/D_g = 10$ of the dilute cases, the temperature distribution still matches very well. For both cases with atomization velocity profiles, the temperature distributions do not show much difference though the D_{32}, D_{10} , and PDF distribution of droplet diameter show a significant difference (see Figs. 6(a) and 7(b)). However, some discrepancies can still be observed, i.e., cases with atomization gas velocity and smaller droplets (Cases 3 and 6) have intermediate values between the cases with flat gas velocity and larger droplets (Cases 1 and 4), and cases with atomization gas velocity and larger droplets (Cases 2 and 5). This is because the turbulence generated by the primary breakup during the atomization process of Cases 3 and 6 (5 mm downstream of the pilot outlet) is weaker than that of Cases 2 and 5 (5 mm upstream of the pilot outlet), but stronger than the flat ones. In addition, the difference disappears when the recess distance is increased from 25 to 80 mm based on a comparison of the differences between a dense spray (Cases 2 and 3) and a dilute spray (Cases 5 and 6) because the ACCs, where the turbulence in the atomization computation is recorded, are 5 mm upstream and 5 mm downstream of the pilot outlet for a dense spray, but are 60 and 50 mm upstream of the pilot outlet for a dilute spray, as shown in Fig. 11. Therefore, the difference in turbulence owing to different ACCs finally disappears at the pilot outlet for a dilute spray.

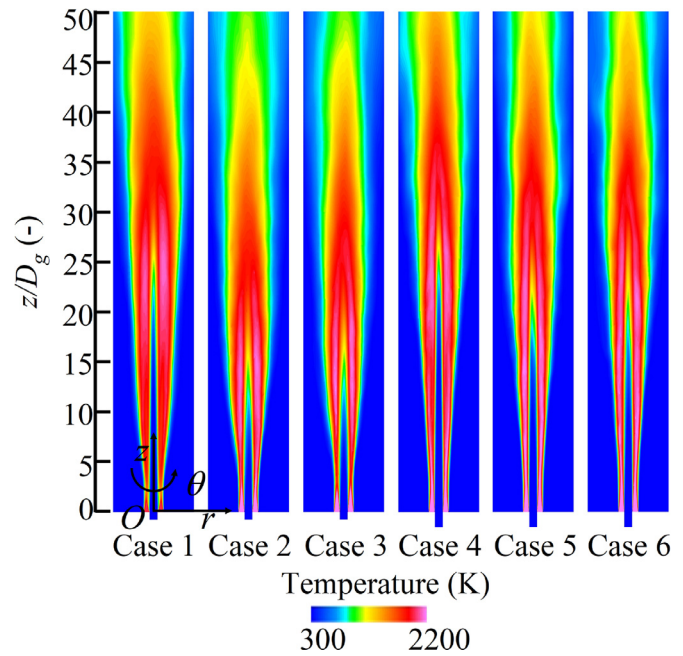


Fig. 15. Comparison of distribution of time-averaged of gas temperature for Cases 1–6.

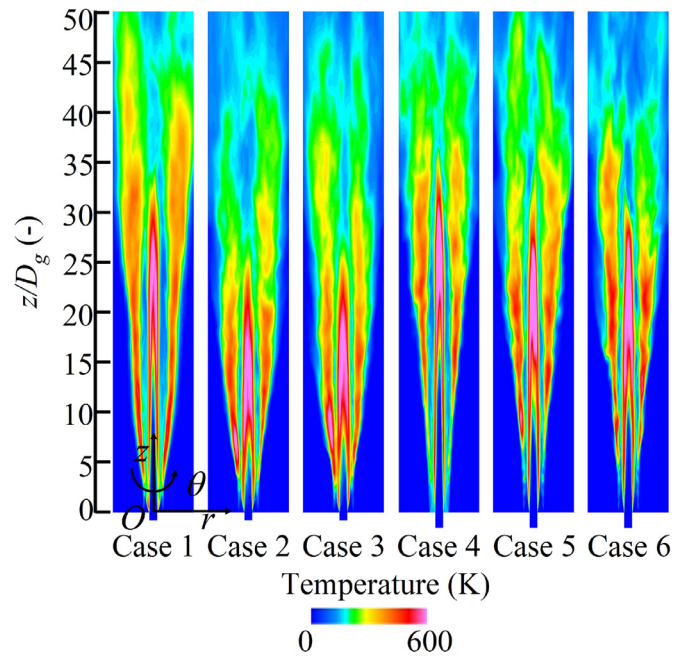


Fig. 16. Comparison of distribution of RMS of gas temperature for Cases 1–6.

An obvious discrepancy is seen between the simulation results and the experimental data at the downstream location of $z/D_g = 20$ of a dense spray, where the temperatures of simulation are overpredicted. In contrast to which, in a dilute spray, the temperature profiles of simulation match those of experiment very well and only drift away at the downstream location of $z/D_g = 20$, which is still not that obvious compared to that in a dense spray. The good agreement in the upstream region is due to the well-controlled boundary conditions which are also the interest of the present study. In addition, a suitable flamelet model or a better combustion mechanism may help to improve the difference observed in the downstream region for the dilute spray. However, for the great discrepancy in the dense spray, the situation is totally

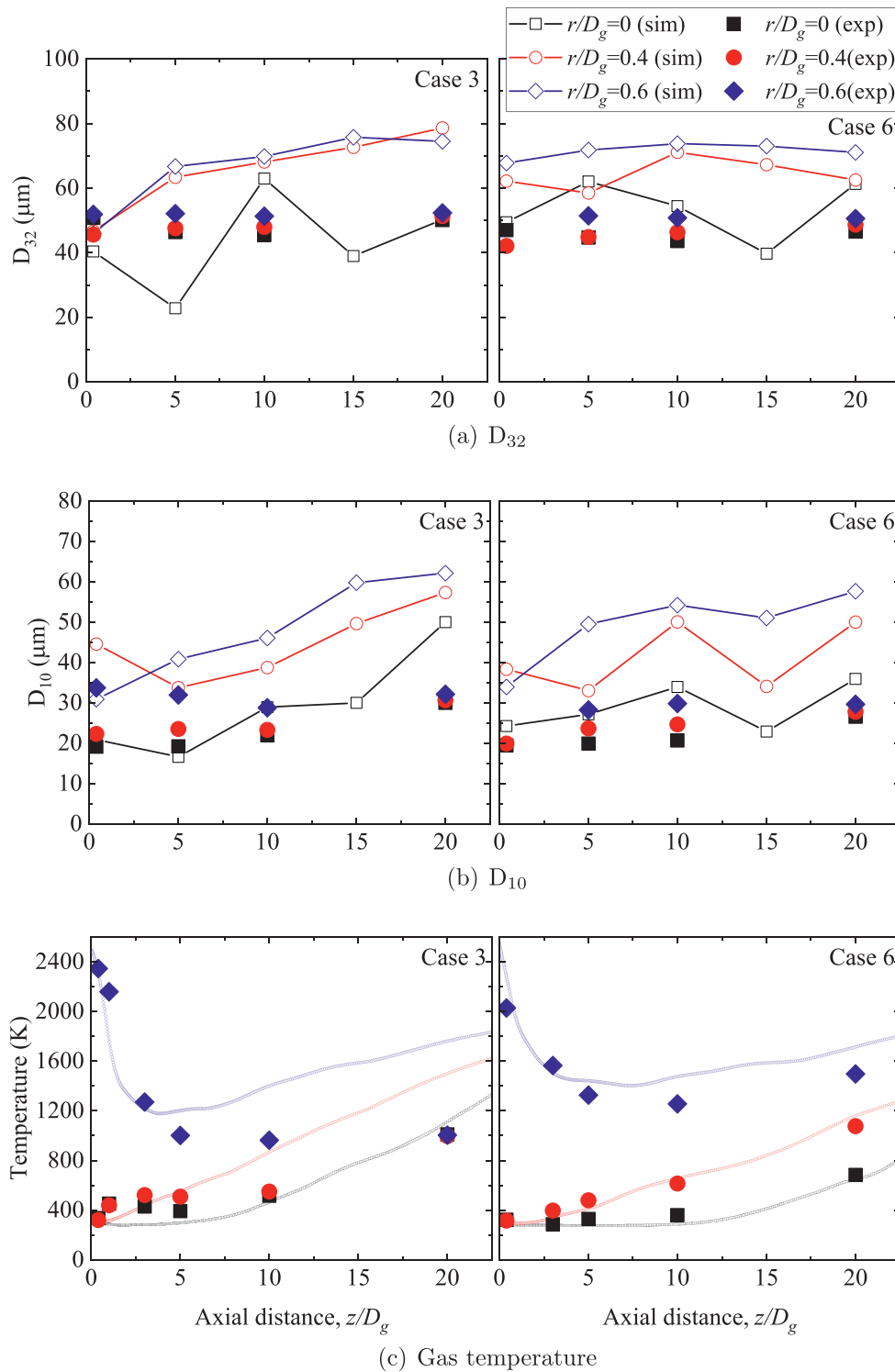


Fig. 17. Comparison of streamwise distributions of time-averaged droplet sizes (D_{32} and D_{10}) and gas temperature at different radial locations of $r/D_g = 0, 0.4,$ and 0.6 between combustion simulation and experiment for Cases 3 and 6. Only droplets diameter less than 0.1 mm are counted.

different. According to the experiment [50], a speculation is proposed that the combustion is finished in the downstream location of $z/D_g = 20$ even there exists fuel droplets that the temperature distribution does not present the symmetric unimodal distribution. On the other hand, the combustion is still happening in the simulation such that an overestimation as well as a totally different structure could be observed. The dense spray region has much more larger ligaments and irregular shaped objects that cannot be

consumed, and those larger liquid components generated by the primary breakup easily cause more unpredicted turbulence when they flow downstream and breakup into smaller droplets. Therefore, the local flow field is extremely unstable in the downstream region, which is different from the upstream region where the disturbances of those ligaments and irregular shaped objects have not developed. Therefore, the burning process might not occur much or just be finished, while the fuel is still present there, resulting in a

lower local temperature distribution. However, in the present simulation, the larger ligaments and irregular shaped objects are just simply transformed into Lagrangian droplets, failing to consider the realistic interaction between the gas phase and liquid fuel, as well as the further breakup behavior. Therefore, the Lagrangian droplets continue to be consumed when they reach further downstream, ensuring a continuous burning without any negative influences on the combustion, and thus a higher temperature distribution could be observed. However, the unstable flow field caused by those ligaments and irregular shaped objects may have significant influences on the fuel droplet evaporation and fuel vapor heat release. Another possibility is that the larger ligaments and irregular shaped objects tend to disperse further in the radial direction and thus the heavier ligaments and irregular shaped objects finally fall when they flow out of the flame zones. However, the total energy of the simulation is conserved such that the temperature distribution of the experiment is lower than that of the simulation.

The profiles of the RMS of gas temperature show a twin peak on the both sides of the centerline until $z/D_g = 10$, which is less distinct for the dense case. This twin peak structure is also well-captured by the present study for all six cases, and the Cases 3 and 6 still have the intermediate values. The computational results show a reasonable match with the experiments near the center axis, and some discrepancies away from the center axis. In the experiment work, the temperature is strongly affected by the pilot flame in the outer space, such that the temperature distribution out of $-1.25 \leq r/D_g \leq 1.25$, outside the edge of the pilot flame, presents some discrepancies. In addition, owing to the larger ligaments and irregular shaped objects mentioned in the last paragraph, it is difficult to capture the accurate temperature distributions in the dense spray cases. Therefore, the discrepancies tend to become eliminated when the recess distance is increased from 25 to 80 mm around the nozzle centerline from $r/D_g = -1$ to $r/D_g = 1$, except for the location at $z/D_g = 20$, where the combustion of dense spray in the experiment is considered to be completed.

Figures 15 and 16 show the distributions of the time-averaged and RMS of gas temperature until the downstream location of $z/D_g = 50$ for all six cases. It can be seen that, compared to the results on the assumption of a uniform inlet boundary condition, the use of inlet velocities determined from the atomization computation can enhance the mixing and establish the combustion at the most upstream locations. On the other hand, the profiles of the fluctuating temperature indicate that the differences of droplets in databases A1 and A4 may not have a significant influence on the combustion characteristics when comparing Cases 2 and 3 as well as Cases 5 and 6. In addition, the symmetrical flame structures in all cases prove that the droplet databases sampled from the atomization computation have no biases in any directions. This confirms that the proposed sampling method coupling the atomization and combustion computations is successful.

Figure 17 shows the streamwise distributions of the time-averaged droplet sizes (D_{32} and D_{10}) and gas temperature of Cases 3 and 6 at different radial locations of $r/D_g = 0, 0.4$, and 0.6 in comparison with the experiment results. Due to the limitation of the experiment measurement of Phase Doppler Anemometry (PDA), the measured droplet size is limited to $100 \mu\text{m}$. Therefore, the calculations of D_{32} and D_{10} omit the Lagrangian droplets with a diameter of larger than $100 \mu\text{m}$. However, the droplet size distributions between simulation and experiment still show large discrepancies, and the discrepancies might result from two reasons from the views of simulation and experiment. From the view of simulation, the E-L transformation utilized in the present study might improperly transform the larger ligaments and irregular shaped objects into Lagrangian droplets leading to an increment in droplet size. From the view of experiment, the PDA has severe criterion to

measure sphere droplets and most sphere droplets holds relatively smaller diameter to maintain the shape, which leads to a decrease in droplet size. However, there are still some shared properties for the droplet size in simulation and experiment. Both D_{32} and D_{10} increase from center to side despite increasing the recess distance from 25 to 80 mm. For the dense spray, the D_{32} values increase slightly further downstream from $z/D_g = 0.4$ –20, whereas for the dilute spray, the D_{32} values decrease slightly from $z/D_g = 10$ –20, which also match the experiment results at the radial locations of $r/D_g = 0.4$ and 0.6 . The D_{10} values of the simulation keep increasing in a dense spray and keep fluctuating in a dilute spray, whereas the D_{10} values of the experiment keep fluctuating in a dense spray and keep increasing in a dilute spray. This opposite development is considered to be a result of omitting the larger Lagrangian droplets artificially. Since D_{10} is more affected by the portion of small droplets, and the measured droplets in the experiment tend to hold smaller diameter whereas the transformed droplets in the simulation may hold larger diameter, hence it is difficult for the simulation to predict the D_{10} values. Regarding the temperature development along with the axial direction, the dilute spray is considered to have a good agreement with the experiment at different radial locations. Whereas, for the dense spray, even good agreement can be observed at the center axis, it fails to capture the downstream temperatures especially for the outer locations of $r/D_g = 0.6$. This is probably because of insufficiency of the consideration of effect of liquid ligaments and irregular shaped objects existing away from the center axis, as mentioned before.

5. Conclusions

In this study, a numerical framework which is a one-way coupling between a VOF simulation and a combustion simulation was proposed, and the validity was investigated for the dense spray flames. Atomization was simulated by a detailed high-resolution VOF simulation, in which both continuum gas and liquid phases were strictly solved in a Eulerian framework, and the Eulerian components of the liquid droplets were transformed into the Lagrangian droplets at a certain downstream cross-section, i.e., sampling cross-section, whose information was stored in the database. Then, the combustion process was solved by a LES/FPV adopting the pre-stored database of Lagrangian droplets (i.e., the position, size, and velocity of each droplet) as the inlet boundary conditions. Computations were validated against measurement made in the Sydney Piloted Needle Spray Burner, which can generate both dilute and dense spray flames by varying the recess distance from the liquid fuel jet nozzle to the pilot outlet.

Regarding the detailed high-resolution VOF simulation of liquid fuel atomization, the volume flux of the droplets at the exit of the nozzle was observed to fluctuate both temporally and spatially, which meant that there exist periods of breakup and non-breakup during the atomization process. It was also found that the breakup period was in good agreement with an existing empirical correlation, and that, compared to the small droplets, larger droplets tended to be located away from the center axis. Meanwhile, in the database of the Lagrangian droplets for the LES/FPV of spray flames, the location of the sampling cross-section, sampling time, and threshold value for a Eulerian–Lagrangian (E-L) transformation were found to strongly affect the properties of the Lagrangian droplets, and to be critical for the success of the use of the LES/FPV of present spray flames.

By use of the optimal pre-stored droplets database, the results of LES/FPV of two flame cases with different recess distances showed generally similar trends with the experiment in terms of the gas temperature and droplet size distributions. The spray flame with a longer recess distance, which represents a dilute spray, was considered to have a longer and wider premixed core than that

with a shorter recess distance representing a dense spray. This behavior is believed to be due to the enhanced mixing between the evaporated fuel and oxidizer. For the dense spray flame, the discrepancy in the gas temperature between the prediction and experiment tended to become more evident, and when moving downstream, the over-predictions were observed. This was considered to be attributed to the fact that for the LES/FPV of the dense spray flame, the relatively large and non-spherical liquid components were regarded as the Lagrangian spherical droplets in the present E-L transformation, and therefore, their further breakup and influence on the turbulence development and flame evolution were neglected.

In summary, the numerical framework proposed in this study is capable of reproducing the spray atomization and the gas temperature distributions in dilute spray flames of Sydney Piloted Needle Burner with a relatively low computational cost and without any atomization model or presumed initial droplet size distribution. Some failures of gas temperature distributions in dense spray flames and droplet size distributions are discussed in detail which requires further investigations. The improvement of the E-L tagging method in generating droplet databases for relatively dense sprays merits future work.

Declaration of Competing Interest

The authors declare that they have no known competing financial interests or personal relationships that could have appeared to influence the work reported in this paper.

Acknowledgments

This work was partially supported by MEXT as “Program for Promoting Researches on the Supercomputer Fugaku” (Digital Twins of Real World’s Clean Energy Systems with Integrated Utilization of Super-simulation and AI) and by JSPS KAKENHI Grant number 19H02076. YH acknowledges the support of the [National Natural Science Foundation of China](#) (Grant no. 52006151) and “the [Fundamental Research Funds for the Central Universities](#)” (YJ201943). AM is supported by the [Australian Research Council](#). The authors also thank Dr. A. Lowe for providing us the detailed configuration of the Sydney Burner.

Appendix A. Details of Chi square homogeneity check for droplet spatial distribution analysis

The homogeneity analysis for droplet spatial distribution is discussed in details. As mentioned in [Section 4.2.2](#), the angle θ in the radial plane and the droplet size can be used to analyze the droplet spatial distribution. The space can be divided into four mathematical quadrants, i.e., $0 \leq \theta < \pi/2$, $\pi/2 \leq \theta < \pi$, $\pi \leq \theta < 3\pi/2$, and $3\pi/2 \leq \theta < 2\pi$, to check the preference in different radial directions, and the droplet size can be divided into three clusters, i.e., 0–50 μm , 50–150 μm , and 150–300 μm to check the distance bias in a certain radial direction. The Chi-square homogeneity validation is a method generally used to analyze the data homogeneity in different clusters, and the data can be regarded as homogeneous if the accumulated value is satisfied. First, the degree of freedom for the Chi-square is calculated as $df = (\text{row} - 1) \times (\text{col} - 1)$, where df indicates the degree of freedom, row is the number of rows, with three droplet size clusters herein; col is the number of columns, i.e., the 4 mathematical quadrants, as shown in [Table 3](#). Therefore, the degree of freedom is $df = (3 - 1) \times (4 - 1) = 6$. The critical value (with 95% confidence level) under a degree of freedom of 6 can be found to be 12.59 according to the statistics, which means that if the total value of all cells is less than 12.59, then the data can be confirmed to have a 95% possibility to ensure the

azimuthal homogeneity of the droplet distribution. The calculation algorithm is very simple, which is briefly introduced. For the cell i in a certain row and column, there is a statistic F_i by counting the number of droplets which satisfy the conditions (i.e., droplet size and angle), and thus a total value of the row or column can be calculated. Based on the statistic of cell i and total values of rows and columns, the expected value of cell i could be calculated as E_i . Then, the total value of all cells, X^2 , of one database can be calculated as $X^2 = \sum_{i=1}^n ((E_i - F_i)^2 / E_i^2)$. By using this Chi-square homogeneity check, if the total value is less than the critical value of 12.59, it can be said that the droplets are homogeneously distributed in the four mathematical quadrants ($0 \leq \theta < \pi/2$, $\pi/2 \leq \theta < \pi$, $\pi \leq \theta < 3\pi/2$, and $3\pi/2 \leq \theta < 2\pi$) with smaller droplets close to the center axis and larger droplets away from the center axial such that the database can be considered to have no special preferences existing in a specific direction.

References

- [1] A.R. Masri, Turbulent combustion of sprays: from dilute to dense, *Combust. Sci. Tech.* 188 (2016) 1619–1639.
- [2] M. Linne, Imaging in the optically dense regions of a spray: a review of developing techniques, *Prog. Energy Combust. Sci.* 39 (2013) 403–440.
- [3] H. Chiu, T. Liu, Group combustion of liquid droplets, *Combust. Sci. Tech.* 17 (1977) 127–142.
- [4] A. Umemura, Interactive droplet vaporization and combustion: approach from asymptotics, *Prog. Energy Combust. Sci.* 20 (1994) 325–372.
- [5] S. Li, Spray stagnation flames, *Prog. Energy Combust. Sci.* 23 (1997) 303–347.
- [6] E. Gutheil, W. Sirignano, Counterflow spray combustion modeling with detailed transport and detailed chemistry, *Combust. Flame* 113 (1998) 92–105.
- [7] A.Y. Klimenko, R.W. Bilger, Conditional moment closure for turbulent combustion, *Prog. Energy Combust. Sci.* 25 (1999) 25–62.
- [8] V. Gopalakrishnan, J. Abraham, Effects of multicomponent diffusion on predicted ignition characteristics of a n-heptane diffusion flame, *Combust. Flame* 136 (2004) 557–566.
- [9] H. Pitsch, M. Ihme, An Unsteady/Flamelet Progress Variable Method for LES of non-Premixed Turbulent Combustion, *AIAA Paper No.* 2005–557.
- [10] J. Reveillon, L. Vervisch, Analysis of weakly turbulent dilute spray flames and spray combustion regimes, *J. Fluid. Mech* 537 (2005) 317–347.
- [11] M. Nakamura, F. Akamatsu, R. Kurose, M. Katsuki, Combustion mechanism of liquid fuel spray in a gaseous flame, *Phys. Fluids* 17 (2005) 1–14.
- [12] J. Reveillon, F.X. Demoulin, Evaporating droplets in turbulent reacting flows, *Proc. Combust. Inst.* 31 (2007) 2319–2326.
- [13] H. Watanabe, R. Kurose, S.M. Huang, F. Akamatsu, Characteristics of flamelets in spray flames formed in a laminar counterflow, *Combust. Flame* 148 (2007) 234–248.
- [14] N. Abani, A. Munnannur, R.D. Reitz, Reduction of numerical parameter dependencies in diesel spray models, *J. Eng. Gas Turbines Power* 130 (2008) 032809.
- [15] Y. Baba, R. Kurose, Analysis and flamelet modelling for spray combustion, *J. Fluid. Mech.* 612 (2008) 45–79.
- [16] M. Ihme, Y.C. See, Prediction of autoignition in a lifted methane / air flame using an unsteady flamelet/progress variable model, *Combust. Flame* 157 (2010) 1850–1862.
- [17] R. Bilger, A mixture fraction framework for the theory and modeling of droplets and sprays, *Combust. Flame* 158 (2011) 191–202.
- [18] K. Luo, H. Pitsch, M.G. Pai, O. Desjardins, Direct numerical simulations and analysis of three-dimensional n-heptane spray flames in a model swirl combustor, *Proc. Combust. Inst.* 33 (2011) 2143–2152.
- [19] M.R. Turner, S.S. Sazhin, J.J. Healey, C. Crua, S.B. Martynov, A breakup model for transient diesel fuel sprays, *Fuel* 97 (2012) 288–305.
- [20] C. Bajaj, M. Ameen, J. Abraham, Evaluation of an unsteady flamelet progress variable model for autoignition and flame lift-off in diesel jets, *Combust. Sci. Tech.* 185 (2013) 454–472.
- [21] S. Ukai, A. Kronenburg, O.T. Stein, LES-CMC of a dilute acetone spray flame, *Proc. Combust. Inst.* 34 (2013) 1643–1650.
- [22] S. De, S.H. Kim, Large eddy simulation of dilute reacting sprays: droplet evaporation and scalar mixing, *Combust. Flame* 160 (2013) 2048–2066.
- [23] S. Tachibana, K. Saito, T. Yamamoto, M. Makida, T. Kitano, R. Kurose, Experimental and numerical investigation of thermos-acoustic instability in a liquid-fuel aero-engine combustor at elevated pressure: validity of large-eddy simulation of spray combustion, *Combust. Flame* 162 (2015) 2621–2637.
- [24] T. Kitano, K. Kaneko, R. Kurose, S. Komori, Large-eddy simulations of gas- and liquid-fueled combustion instabilities in back-step flows, *Combust. Flame* 170 (2016) 63–78.
- [25] L. Ma, D. Roekaerts, Numerical study of the multi-flame structure in spray combustion, *Proc. Combust. Inst.* 36 (2017) 2603–2613.
- [26] B. Wang, A. Kronenburg, G.L. Tufano, O.T. Stein, Fully resolved DNS of droplet array combustion in turbulent convective flows and modelling for mixing field in inter-droplet space, *Combust. Flame* 189 (2018) 347–366.
- [27] A. Pillai, R. Kurose, Combustion noise analysis of a turbulent spray flame using a hybrid DNS/APE-RF approach, *Combust. Flame* 200 (2019) 168–191.

- [28] Y. Hu, R. Kurose, Nonpremixed and premixed flamelets LES of partially premixed spray flames using a two-phase transport equation of progress variable, *Combust. Flame* 188 (2018) 227–242.
- [29] Y. Hu, R. Kurose, Partially premixed flamelet in LES of acetone spray flames, *Proc. Combust. Inst.* 37 (2019) 3327–3334.
- [30] Y. Hu, R. Kai, R. Kurose, E. Gutheil, H. Olguin, Large eddy simulation of a partially pre-vaporized ethanol reacting spray using the multiphase DTF/flamelet model, *Int. J. Multiph. Flow* 125 (2020) 103216.
- [31] Y. Hardalupas, A. Taylor, J.H. Whitelaw, Mass flux, mass fraction and concentration of liquid fuel in a swirl-stabilized flame, *Int. J. Multiph. Flow* 20 (1994) 233–259.
- [32] G. Chen, A. Gomes, Dilute laminar spray diffusion flames near the transition from group combustion to individual droplet burning, *Combust. Flame* 110 (1997) 392–404.
- [33] M. Alden, J. Bood, Z. Li, M. Richter, Visualization and understanding of combustion processes using spatially and temporally resolved laser diagnostic techniques, *Proc. Combust. Inst.* 33 (2011) 69–97.
- [34] D. Cavaliere, J. Kariuki, E. Mastorakos, A comparison of the blow-off behaviour of swirl-stabilized premixed, non-premixed and spray flames, *Flow Turbul. Combust.* 91 (2013) 347–372.
- [35] M. Chrigui, J. Gounder, A. Sadiki, J. Janicka, A.R. Masri, Acetone droplet behavior in reacting and non reacting turbulent flow, *Flow Turbul. Combust.* 90 (2013) 419–447.
- [36] H. Luo, K. Nishida, S. Uchitomi, Y. Ogata, W. Zhang, T. Fujikawa, Effect of temperature on fuel adhesion under spray-wall impingement condition, *Fuel* 234 (2018) 56–65.
- [37] A. Verdier, J.M. Santiago, A. Vandel, G. Godard, G. Cabot, B. Renou, Local extinction mechanisms analysis of spray jet flame using high speed diagnostics, *Combust. Flame* 193 (2018) 440–452.
- [38] I.A. Mulla, G. Godard, G. Cabot, F. Grisch, B. Renou, Quantitative imaging of nitric oxide concentration in a turbulent -heptane spray flame, *Combust. Flame* 203 (2019) 217–229.
- [39] D.R. Guildenbecher, C. Lopez-Rivera, P.E. Sojka, Secondary atomization, *Exp. Fluids* 46 (2009) 371–402.
- [40] X. Jiang, G. Siamas, K. Jagus, T. Karyiannis, Physical modelling and advanced simulations of gas-liquid two-phase jet flows in atomization and sprays, *Prog. Energy Combust. Sci.* 36 (2010) 131–167.
- [41] M. Herrmann, Detailed numerical simulations of the primary atomization of a turbulent liquid jet in crossflow, *J. Eng. Gas Turbines Power* 132 (2010) 061506.
- [42] N. Ashgriz, Atomization of a liquid jet in a crossflow, *AIP Conf. Proc.* 1440 (2012) 33–46.
- [43] X. Li, M.C. Soteriou, Detailed numerical simulation of liquid jet atomization in crossflow of increasing density, *Int. J. Multiph. Flow* 104 (2018) 214–232.
- [44] A. Umemura, J. Shinjo, Detailed SGS atomization model and its implementation to two-phase flow LES, *Combust. Flame* 195 (2018) 232–252.
- [45] T.-W. Lee, J.E. Park, R. Kurose, Determination of the drop size during atomization and liquid jets in cross flows, *At. Sprays* 28 (2018) 241–254.
- [46] J. Wen, Y. Hu, A. Nakanishi, R. Kurose, Atomization and evaporation process of liquid fuel jets in crossflows: a numerical study using Eulerian/Lagrangian method, *Int. J. Multiph. Flow* 129 (2020) 103331.
- [47] A. Pillai, J. Nagao, R. Awane, R. Kurose, Influences of liquid fuel atomization and flow rate fluctuations on spray combustion instabilities in a backward-facing step combustor, *Combust. Flame* 220 (2020) 337–356.
- [48] J.D. Gounder, A. Kourmatzis, A.R. Masri, Turbulent piloted dilute spray flames: flow fields and droplet dynamics, *Combust. Flame* 159 (2012) 3372–3397.
- [49] L.M. Thomas, A. Lowe, A. Satija, A.R. Masri, R.P. Lucht, Five kHz thermometry in turbulent spray flames using chirped-probe pulse femtosecond CARS, part I: processing and interference analysis, *Combust. Flame* 200 (2019) 405–416.
- [50] A. Lowe, L.M. Thomas, A. Satija, R.P. Lucht, A.R. Masri, Five kHz thermometry in turbulent spray flames using chirped-probe pulse femtosecond CARS, part II: structure of reaction zones, *Combust. Flame* 200 (2019) 417–432.
- [51] H. Moriai, R. Kurose, H. Watanabe, Y. Yano, F. Akamatsu, S. Komori, Large-eddy simulation of turbulent spray combustion in a subscale aircraft jet engine combustor-predictions of NO and soot concentrations, *J. Eng. Gas Turbines Power* 135 (2013) 091503.
- [52] A. Kishimoto, H. Moriai, K. Takenaka, T. Nishiie, M. Adachi, A. Ogawara, R. Kurose, Application of a non-adiabatic flamelet/progress-variable approach to large eddy simulation of H₂/O₂ combustion under a pressurized condition, *J. Heat Transf.* 139 (2017) 124501.
- [53] J.U. Brackbill, D.B. Kothe, C. Zemach, A continuum method for modeling surface tension, *J. Comput. Phys.* 100 (1992) 335–354.
- [54] S. Muzaferija, M. Peric, Computation of free-surface flows using interface-tracking and interface-capturing methods, in: O. Mahrenholtz, M. Markiewicz (Eds.), *Nonlinear Water Wave Interaction*, Computational Mechanics Publications, Southampton (1998), pp. 59–100.
- [55] A. Albadawi, D.B. Donoghue, A.J. Robinson, D.B. Murray, Y.M.C. Delauré, Influence of surface tension implementation in volume of fluid and coupled volume of fluid with level set methods for bubble growth and detachment, *Int. J. Multiph. Flow* 53 (2013) 11–28.
- [56] M. Herrmann, A parallel Eulerian interface tracking/Lagrangian point particle multi-scale coupling procedure, *J. Comput. Phys.* 229 (2010) 745–759.
- [57] C.D. Pierce, P. Moin, Progress-variable approach for large-eddy simulation of non-premixed turbulent combustion, *J. Fluid Mech.* 504 (2004) 73–97.
- [58] N. Lallemand, A. Sayre, R. Weber, Evaluation of emissivity correlations for H₂O-CO₂-N₂/air mixtures and coupling with solution methods of the radiative transfer equation, *Prog. Energy Combust.* 22 (1996) 543–574.
- [59] H. Pitsch, H. Steiner, Large-eddy simulation of a turbulent piloted methane/air diffusion flame (Sandia flame D), *Phys. Fluids* 12 (2000) 2541.
- [60] D.K. Lilly, A proposed modification of the Germano subgrid-scale closure method, *Phys. Fluids A* 4 (1992) 633–635.
- [61] C.T. Crowe, M.P. Sharma, D.E. Stock, The particle-source-in cell (PSI-CELL) model for gas-droplet flows, *J. Fluid Eng. Trans. ASME* 99 (1977) 325–332.
- [62] R.S. Miller, K. Harstad, J. Bellan, Evaluation of equilibrium and non-equilibrium evaporation models for many-droplet gas-liquid flow simulations, *Int. J. Multiph. Flow* 24 (1998) 1025–1055.
- [63] R. Kurose, H. Makino, S. Komori, M. Nakamura, F. Akamatsu, M. Katsuki, Effects of outflow from the surface of a sphere on drag, shear lift, and scalar diffusion, *Phys. Fluids* 15 (2003) 2338–2351.
- [64] T. Kitano, J. Nishio, R. Kurose, S. Komori, Evaporation and combustion of multicomponent fuel droplets, *Fuel* 136 (2014) 219–225.
- [65] T. Kitano, J. Nishio, R. Kurose, S. Komori, Effects of ambient pressure, gas temperature and combustion reaction on droplet evaporation, *Combust. Flame* 161 (2014) 551–564.
- [66] P.J. O'Rourke, A.A. Amsden, The TAB Method for Numerical Calculation of Spray Droplet Breakup, SAE Paper, 1987.
- [67] H. Pitsch, *Flamemaster: a C++ computer program for 0D combustion and 1D laminar flame calculations*, Cited in, 1998, p. 81.
- [68] S. Pichon, G. Black, N. Chaumeix, M. Yahyaoui, J.M. Simmie, H.J. Curran, R. Donohue, The combustion chemistry of a fuel tracer: measured flame speeds and ignition delays and a detailed chemical kinetic model for the oxidation of acetone, *Combust. Flame* 156 (2009) 494–504.
- [69] D. Zuzio, J.E. ezés, B. DiPierro, An improved multiscale Eulerian–Lagrangian method for simulation of atomization process, *Comput. Fluids* 176 (2018) 285–301.
- [70] S. Elghobashi, Particle-laden turbulent flows: direct simulation and closure models, *Appl. Sci. Res.* 48 (1991) 301–314.
- [71] J.-P. Matas, S. Marty, A. Cartellier, Experimental and analytical study of the shear instability of a gas-liquid mixing layer, *Phys. Fluids* 23 (2011) 094112.
- [72] J.-P. Matas, A. Delon, A. Cartellier, Shear instability of an axisymmetric air-water coaxial jet, *J. Fluid Mech.* 843 (2018) 575–600.